Title

Joint scheduling of energy, fast and primary frequency response reserves in integrated transmission—distribution networks

Journal

International Journal of Electrical Power & Energy Systems, 177

ISSN

0142-0615

Authors

Noh, Seung-Gil
Heleno, Miguel
Choi, Woo Yeong
et al.

Publication Date

2026-04-01

DOI

10.1016/j.ijepes.2026.111892

Electrical Power and Energy Systems 177 (2026) 111892

Contents lists available at ScienceDirect

International Journal of Electrical Power and Energy Systems

journal homepage: www.elsevier.com/locate/ijepes

Joint scheduling of energy, fast and primary frequency response reserves in integrated transmission–distribution networks

Seung-Gil Noh [a], Miguel Heleno [b], Woo Yeong Choi [c], Yun-Su Kim [d],*

[a] Graduate School of Energy Convergence, Gwangju Institute of Science and Technology, 123 Cheomdan-gwagiro, Buk-gu, Gwangju, 61005, Republic of Korea
[b] Lawrence Berkeley National Laboratory, 1 Cyclotron Road, Berkeley, CA, 94720, USA
[c] Distributed Power System Research Center, Korea Electrotechnology Research Institute, 27 Dosicheomdansaneop-ro, Gwangju, 61751, Republic of Korea
[d] Department of Electrical Engineering and Computer Science, Gwangju Institute of Science and Technology, 123 Cheomdan-gwagiro, Buk-gu, Gwangju, 61005, Republic of Korea

ARTICLE INFO

Keywords:
Bi-level optimization
Transmission–distribution coordination
Power system scheduling
Energy and reserve dispatch
Fast frequency response
Primary frequency response

ABSTRACT

Inverter-based distributed energy resources (DERs) connected to distribution networks (DNs) can provide fast frequency support, but their reserve deliverability depends on feeder constraints and differs from synchronous primary frequency response (PFR). Existing transmission–distribution coordination studies usually treat reserve generically or neglect feeder-level feasibility, while frequency-security scheduling studies rarely represent distribution feeders explicitly. This paper develops a bi-level day-ahead scheduling framework for integrated transmission–distribution networks that jointly clears energy, transmission-side PFR, and distribution-side fast frequency response (FFR) under exogenous hourly inertia and largest-loss inputs from an external unit commitment (UC) schedule. The transmission problem is modeled with DC-optimal power flow (OPF) and closed-form second-order cone (SOC) frequency-security constraints, whereas each DN is represented by a reserve-aware branch-flow AC-OPF so that scheduled fast reserves remain deliverable during activation. The bi-level problem is reformulated through Karush–Kuhn–Tucker (KKT) conditions into a mixed-integer SOC program, and a penalty term is used to tighten the distribution-network relaxation. In the reduced test system, lower exogenous inertia increased the required primary response from 179.64 MW to 191.08 MW, distribution-side fast response reduced total frequency-response procurement by up to 4.9%, and neglecting distribution constraints overstated the combined distribution-side energy and reserve award by up to 18%. In the expanded study, the largest case was solved in 2.02 s with a 0.00% optimality gap. Time-domain simulations kept the frequency nadir above 59.0 Hz in all tested hours. These results demonstrate the value of fast-response modeling and distribution-feasible reserve delivery in coordinated market clearing.

1. Introduction

1.1. Background and motivation

As the deployment of distributed energy resources (DERs) continues to accelerate, their growing role in system flexibility has been discussed in [1]. Their role in contingency frequency services was studied in [2], and broader flexibility implications under high renewable penetration were reviewed in [3]. For photovoltaic systems (PVs), [4] demonstrated advanced grid-friendly controls. For wind resources, market participation was examined in [5], frequency control in autonomous systems in [6], reserve policy optimization in [7], and frequency-constrained planning with wind support in [8]. However, unlike conventional synchronous generators, most DERs are connected to distribution networks (DNs), are dispersed across feeders, and exhibit dynamic characteristics that differ from those of transmission network (TN) resources. Their reserve capability therefore cannot be assessed only at the bulk-system level.

In parallel, the operational role of the DN is shifting from passive power reception to active coordination of DERs, flexible demand, and reserve provision. Related energy-management studies have addressed both network operation and longer-term power-network planning problems [9,10]. This evolution makes coordination between the TN and DNs increasingly important, because energy and reserve exchanges at the points of common coupling (PCC) must remain consistent with the physical constraints of both networks. Existing transmission–distribution coordination studies have addressed several

* Corresponding author.
E-mail addresses: seunggil@gm.gist.ac.kr (S.-G. Noh), miguelheleno@lbl.gov (M. Heleno), choiwy@keri.re.kr (W.Y. Choi), yunsukim@gist.ac.kr (Y.-S. Kim).

https://doi.org/10.1016/j.ijepes.2026.111892
Received 3 November 2025; Received in revised form 23 March 2026; Accepted 25 April 2026
Available online 30 April 2026

Nomenclature

Sets and Indices

$\mathcal{B}^{\mathrm{T/D}}$	Set of buses in the TN/DN, indexed by i
$\mathcal{L}^{\mathrm{T/D}}$	Set of lines in the TN/DN, indexed by l or ij
$\mathcal{G}^{\mathrm{T/D}}$	Subset of buses in the TN/DN with connected generator, indexed by i
$\mathcal{D}^{\mathrm{T/D}}$	Subset of buses in the TN/DN with connected demand, indexed by i
$\mathcal{I}$	Subset of interface buses between the TN and the DNs, indexed by s
$\mathcal{P}_i$	Subset of parent buses at bus i
$\mathcal{C}_i$	Subset of child buses at bus i
$\mathcal{T}$	Set of time periods, indexed by t
$\Xi^{[\cdot]}$	Set of decision variables, where $[\cdot]$ denotes the upper-level (UL), lower-level (LL), and single-level reformulation of the MPEC model (SL)

Parameters

Transmission Side:

$\overline{P}_i, \underline{P}_i$	Upper/lower bound of active power for the generator connected to bus i
$\overline{L}_l$	Upper bound of active power for line l
$\overline{P}_i^{\mathrm{PFR}}$	Upper bound of PFR for the generator connected to bus i
$P_{i,t}^{\mathrm{d}}$	Active power demand at bus i at time t
γ_{li}	Generation shift factor between bus i and line l
f_0	Nominal power system frequency
$\Delta\overline{f}$	Maximum allowable frequency deviation at the nadir
t^{FFR}	FFR delivery time of the generator
t^{PFR}	PFR delivery time of the generator
H_t^{sys}	System inertia at time t
P_t^{loss}	Single largest generation loss under the $N-1$ criterion at time t, defined as the rated capacity of the largest online synchronous generator.
$C_{i,t}$	Offer price for the active power output of the generator connected to bus i at time t
$C_{i,t}^{\mathrm{PFR}}$	Offer price for the PFR of the generator connected to bus i at time t
$C_{0,t,s}$	Offer price for the active power transaction at PCC s at time t
$C_{0,t,s}^{\mathrm{FFR}}$	Offer price for the FFR transaction at PCC s at time t

Distribution Side:

$\overline{V}_{i,s}, \underline{V}_{i,s}$	Upper/lower bound of voltage magnitude at bus i
$\overline{P}_{i,s}, \underline{P}_{i,s}$	Upper/lower bound of active power for the generator connected to bus i
$\overline{Q}_{i,s}, \underline{Q}_{i,s}$	Upper/lower bound of reactive power for the generator connected to bus i
$\overline{P}_{i,s}^{\mathrm{FFR}}$	Upper bound of FFR for the generator connected to bus i
$R_{ij,s}$	Series resistance for line ij
$X_{ij,s}$	Series reactance for line ij
$\overline{L}_{ij,s}$	Upper bound of current for line ij
$P_{i,t,s}^{\mathrm{d}}$	Active power demand at bus i at time t
$Q_{i,t,s}^{\mathrm{d}}$	Reactive power demand at bus i at time t
$C_{i,t,s}$	Offer price for the active power output of the generator connected to bus i at time t
$C_{i,t,s}^{\mathrm{FFR}}$	Offer price for the FFR of the generator connected to bus i at time t

Variables

Transmission Side:

$p_{i,t}$	Active power output for the generator connected to bus i at time t
$p_{i,t}^{\mathrm{PFR}}$	Available headroom of the generator connected to bus i for PFR at time t

Distribution Side:

$p_{i,t,s}$	Active power output for the generator connected to bus i at time t, with $i = 0$ denoting the net active-power transaction at the PCC bus of DN s
$q_{i,t,s}$	Reactive power output for the generator connected to bus i at time t, with $i = 0$ denoting the net reactive-power transaction at the PCC bus of DN s
$v_{i,t,s}$	Squared voltage magnitude at bus i at time t
$p_{ij,t,s}$	Active power flow for line ij at time t
$q_{ij,t,s}$	Reactive power flow for line ij at time t
$\ell_{ij,t,s}$	Squared current magnitude for line ij at time t
$p_{i,t,s}^{\mathrm{FFR}}$	Available headroom of the generator connected to bus i for FFR at time t, with $i = 0$ denoting the FFR transaction at the PCC bus of DN s
$v_{i,t,s}^{*}$	Squared voltage magnitude at bus i at time t under reserve activation
$p_{ij,t,s}^{*}$	Active power flow for line ij at time t under reserve activation
$q_{ij,t,s}^{*}$	Reactive power flow for line ij at time t under reserve activation
$\ell_{ij,t,s}^{*}$	Squared current magnitude for line ij at time t under reserve activation

aspects of this problem. A bi-level equilibrium problem with equilibrium constraints (EPEC)-based distribution market-clearing framework was developed in [11]. Joint energy and flexibility clearing with explicit TN–DN coordination was studied in [12], while uncertainty-aware active distribution network (ADN) participation at the TN–DN interface was examined in [13]. A non-cooperative operating framework between the TN and DNs was reported in [14]. Although these studies advance coordinated scheduling and pricing, they generally represent flexibility or reserve products in an aggregated manner and do not explicitly distinguish the dynamic value of fast inverter-based response from slower primary response delivered by synchronous units.

A complementary stream of research has focused on frequency security and reserve heterogeneity. Closed-form frequency-security constraints for distinct services were developed in [15], and marginal pricing of inertia and frequency response (FR) with diverse dynamics was studied in [16]. The participation of renewable and inverter-based resources in inertia and reserve provision was further examined in [17]. In addition, [18] presented a bi-level market-design framework in which aggregated virtual power plants (VPPs) provide inertia and frequency-response services to a frequency-constrained unit commitment (FCUC) model. A recent study [19] addressed integrated TN–DN operation with frequency-security constraints in a two-stage robust FCUC framework. Nevertheless, these studies remain centered on unit commitment (UC) formulations and do not explicitly enforce feeder-level network feasibility for DN-side reserve delivery, nor do they quantify the scheduling distortion caused by neglecting DN operational constraints. As DER penetration grows, both TN congestion and DN feeder constraints can materially affect whether the reserve awarded at the interface is actually deliverable [20,21].

Table 1
Positioning of the proposed framework relative to representative TN–DN coordination and frequency-security studies.

Ref.	TN Model	DN/VPP Model	UC	DN reserve Deliverability	Inertia	FFR	PFR	Frequency Security	Interface (TN–DN/VPP)	Interface Signals
Coordination Studies										
[11]	✓	✓	–	–	–	–	–	–	✓	✓
[12]	✓	✓	–	△	–	–	–	–	✓	✓
[13]	✓	✓	–	△	–	–	–	–	✓	✓
[22]	✓	△	–	–	–	–	–	△	✓	✓
[23]	✓	✓	–	–	–	–	–	–	✓	✓
[24]	✓	✓	–	–	–	–	–	–	✓	✓
[25]	✓	△	–	–	–	–	–	–	✓	✓
[26]	✓	△	–	△	–	–	–	–	✓	✓
[27]	△	✓	–	✓	–	–	–	–	✓	✓
[28]	✓	✓	–	△	–	–	–	–	✓	✓
Frequency-security Studies										
[15]	△	–	✓	–	✓	✓	✓	✓	–	–
[16]	△	–	✓	–	✓	✓	✓	✓	–	–
[17]	△	△	✓	–	✓	✓	✓	✓	–	–
[18]	△	△	✓	–	✓	✓	✓	✓	✓	✓
[29]	△	–	✓	–	✓	–	✓	✓	–	–
[30]	△	–	△	–	✓	✓	✓	✓	–	–
This work	✓	✓	△	✓	✓	✓	✓	✓	✓	✓

Note. ✓ denotes features explicitly modeled in the main formulation, △ denotes partial, indirect, aggregated, or exogenous treatment, and – denotes not considered. For the proposed work, UC is marked △ because hourly inertia and largest-loss values are taken from an external UC stage instead of being co-optimized inside the bilevel clearing model.

These gaps motivate the present study. The problem addressed here is a coordinated day-ahead market-clearing and economic-dispatch (ED) problem with exogenous commitment-dependent security inputs. More specifically, the hourly system inertia and largest-loss parameters are obtained from an external UC stage and treated as inputs to the coordinated energy-and-reserve scheduling model. The focus is therefore not endogenous UC, but the physically feasible co-scheduling of energy, primary frequency response (PFR), and fast frequency response (FFR) across the TN and DNs under a consistent market interface. Table 1 compares representative studies on transmission–distribution coordination and frequency-security scheduling with the proposed framework.

1.2. Scope and contributions

This paper develops a bi-level joint scheduling framework for integrated TN–DN operation under distinct frequency-response services. The main contributions are as follows.

(i) A coordinated day-ahead market-clearing model is formulated for energy and reserve scheduling across the TN and DNs while respecting the distinct network constraints of the two layers. In contrast to formulations that aggregate reserve products, the proposed model distinguishes TN-side PFR from DN-side FFR according to their delivery times and dynamic characteristics.
(ii) A closed-form second-order cone (SOC) frequency-security representation is embedded in the TN market-clearing problem to capture nadir-related reserve requirements under exogenous hourly inertia and largest-loss inputs. At the same time, each DN is modeled with a reserve-aware branch-flow AC-optimal power flow (OPF) so that energy dispatch and FFR awards remain physically deliverable during reserve activation.
(iii) To solve the proposed coordinated formulation tractably, the bi-level model is reformulated as a mathematical program with equilibrium constraints (MPEC) and converted into a mixed-integer second-order cone program (MISOCP) through standard Karush–Kuhn–Tucker (KKT)-based reformulation and linearization, while a penalty term is used to tighten the DN second-order cone programming (SOCP) relaxation with limited impact on the market-clearing results.
(iv) The case studies are organized to validate both mechanism and applicability. The reduced-system study shows how exogenous inertia changes PFR needs, how explicit DN-side FFR reduces total reserve procurement, and how neglecting DN network constraints leads to spurious DER energy and reserve awards. The expanded multi-DN study examines scalability, operating-cost outcomes, and relaxation gaps. Finally, PSS/E time-domain simulations verify that the scheduled reserves achieve the intended frequency behavior, including a no-FFR severe hour and FFR-supported hours that yield similar nadirs under different inertia conditions.

To visually summarize these contributions, Fig. 1 presents a graphical overview of the proposed coordinated TN–DN day-ahead scheduling framework, showing the exogenous commitment-dependent security inputs from the external UC stage, the PCC-based exchange of energy and reserve, and the differentiated roles of TN-side PFR and DN-side FFR.

1.3. Paper structure

The remainder of this paper is organized as follows. Section 2 describes the integrated TN–DN framework and the associated modeling assumptions. Section 3 presents the bi-level problem formulation, including the energy, network, and frequency-security constraints. Section 4 explains the MPEC reformulation, the mixed-integer SOC transformation, and the penalty-based relaxation-tightening procedure. Section 5 reports the reduced-system case studies, the expanded-system results, and the time-domain validation. Section 6 concludes the paper and discusses limitations and future research directions.

2. Framework and assumptions

The integrated system structure composed of the TN and DNs is illustrated in Fig. 2. The TN consists of the set of buses $\mathcal{B}^{\mathrm{T}}$, the set of lines $\mathcal{L}^{\mathrm{T}}$, the subset of buses with generators $\mathcal{G}^{\mathrm{T}}$, and the subset of buses with demands $\mathcal{D}^{\mathrm{T}}$. It is modeled using the load demand $P^{\mathrm{d}}_{i,t}$, generator output $p_{i,t}$, and the PFR $p^{\mathrm{PFR}}_{i,t}$ from generators. The DN consists of the set of buses $\mathcal{B}^{\mathrm{D}}$, the set of lines $\mathcal{L}^{\mathrm{D}}$, the subset of buses with DERs $\mathcal{G}^{\mathrm{D}}$, and the subset of buses with demands $\mathcal{D}^{\mathrm{D}}$. It is modeled using active and reactive load demands $P^{\mathrm{d}}_{i,t,s}$ and $Q^{\mathrm{d}}_{i,t,s}$, DER output $p_{i,t,s}$, and FFR

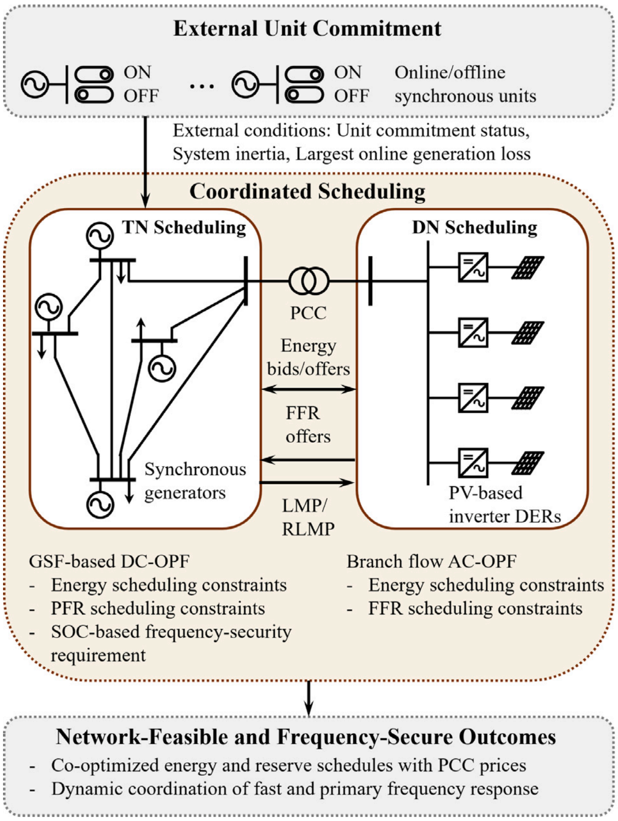

Fig. 1. Graphical overview of the proposed coordinated TN–DN day-ahead scheduling framework with exogenous commitment-dependent security inputs and PCC-based energy and reserve coordination.

$p^{\mathrm{FFR}}_{i,t,s}$ from DERs. The reserves considered in this study are operational reserves required to satisfy the N-1 contingency criterion.

These requirements vary depending on system operating conditions, resource composition, and the dynamic characteristics of individual resources [15,16]. To meet these requirements, conventional TN resources provide PFR, while inverter-based DN resources, which are assumed to be PV units in this study, offer FR services with faster response times. Although various terms are used for this fast response reserve [31], it is referred to as FFR in this paper. The interconnection between each DN and the TN is represented by an index $s \in \mathcal{I}$, where each s denotes a DN connected to a specific TN bus. These connection points represent the PCC between the TN and DNs.

Based on this system structure, the present study considers a coordinated day-ahead market-clearing and ED setting in which the TN and the DNs are operated by independent entities, and each DN is represented by a single DN-side coordinator interfacing with the TN at the PCC [32–34]. In the lower-level (LL) model, the TN clears energy and reserve together with PCC transactions, while in the upper-level (UL) model, the DN-side coordinator schedules DN-side energy and FFR based on the PCC locational marginal price (LMP), reserve locational marginal price (RLMP), and DN resource bids and offers. Because the cleared PCC quantities and the corresponding price signals are mutually dependent, the TN–DN interaction is represented through an equilibrium-based coordination framework [35]. In the present formulation, the interface variables are the PCC energy and FFR transactions, $p_{0,t,s}$ and $p^{\mathrm{FFR}}_{0,t,s}$, together with the associated LMP and RLMP signals.

The coordinated model is developed as an analytical day-ahead clearing framework. DN-side bids and feeder constraints are represented explicitly in the formulation, so privacy-preserving coordination is not addressed in the present study.

3. Problem formulation

As discussed in Section 2, the integrated scheduling model for energy and reserve procurement is formulated as a bi-level optimization framework. In the UL model, the DN schedules energy and reserve by considering the characteristics of resources connected to the DN. In the LL model, the TN is scheduled by reflecting the decisions and capabilities of TN connected resources. During this process, energy and reserve exchanges between the TN and DN occur simultaneously, and the associated prices are determined based on the LMP and RLMP results derived from TN operational scheduling. The details are as follows:

$$\min_{\Xi^{\mathrm{UL}}} \sum_{t\in\mathcal{T}}\sum_{s\in\mathcal{I}}\Bigg(\pi^{\mathrm{LMP}}_{0,t,s}\,p_{0,t,s} + \pi^{\mathrm{RLMP}}_{0,t,s}\,p^{\mathrm{FFR}}_{0,t,s} + \sum_{i\in\mathcal{G}^{\mathrm{D}}}\big(C_{i,t,s}p_{i,t,s} + C^{\mathrm{FFR}}_{i,t,s}p^{\mathrm{FFR}}_{i,t,s}\big)\Bigg) \tag{1a}$$

$$\text{s.t.}\;\; p_{i,t,s} - P^{\mathrm{d}}_{i,t,s} = \sum_{j\in C_{i,t,s}} p_{ij,t,s} - \big(p_{\mathcal{P}_i i,t,s} - R_{\mathcal{P}_i,s}\ell_{\mathcal{P}_i i,t,s}\big),\;\; i\in\mathcal{B}^{\mathrm{D}},\forall t,s, \tag{1b}$$

$$q_{i,t,s} - Q^{\mathrm{d}}_{i,t,s} = \sum_{j\in C_{i,t,s}} q_{ij,t,s} - \big(q_{\mathcal{P}_i i,t,s} - X_{\mathcal{P}_i,s}\ell_{\mathcal{P}_i i,t,s}\big),\;\; i\in\mathcal{B}^{\mathrm{D}},\forall t,s, \tag{1c}$$

$$v_{j,t,s} = v_{i,t,s} - 2\big(R_{ij,s}p_{ij,t,s} + X_{ij,s}q_{ij,t,s}\big) + \big(R^2_{ij,s} + X^2_{ij,s}\big)\ell_{ij,t,s},\;\; ij\in\mathcal{L}^{\mathrm{D}},\forall t,s, \tag{1d}$$

$$0 \le \ell_{ij,t,s} \le \overline{L}^2_{ij,s},\;\; ij\in\mathcal{L}^{\mathrm{D}},\forall t,s, \tag{1e}$$

$$\underline{V}^2_{i,s} \le v_{i,t,s} \le \overline{V}^2_{i,s},\;\; i\in\mathcal{B}^{\mathrm{D}},\forall t,s, \tag{1f}$$

$$\underline{P}_{i,s} \le p_{i,t,s} \le \overline{P}_{i,s},\;\; i\in\mathcal{G}^{\mathrm{D}},\forall t,s, \tag{1g}$$

$$\underline{Q}_{i,s} \le q_{i,t,s} \le \overline{Q}_{i,s},\;\; i\in\mathcal{G}^{\mathrm{D}},\forall t,s, \tag{1h}$$

$$\left\|\begin{matrix} 2p_{ij,t,s} \\ 2q_{ij,t,s} \\ \ell_{ij,t,s} - v_{i,t,s}\end{matrix}\right\|_2 \le \ell_{ij,t,s} + v_{i,t,s},\;\; ij\in\mathcal{L}^{\mathrm{D}},\forall t,s, \tag{1i}$$

$$p_{i,t,s} + p^{\mathrm{FFR}}_{i,t,s} - P^{\mathrm{d}}_{i,t,s} = \sum_{j\in C_{i,t,s}} p^{*}_{ij,t,s} - \big(p^{*}_{\mathcal{P}_i i,t,s} - R_{\mathcal{P}_i,s}\ell^{*}_{\mathcal{P}_i i,t,s}\big),\;\; i\in\mathcal{B}^{\mathrm{D}},\forall t,s, \tag{1j}$$

$$q_{i,t,s} - Q^{\mathrm{d}}_{i,t,s} = \sum_{j\in C_{i,t,s}} q^{*}_{ij,t,s} - \big(q^{*}_{\mathcal{P}_i i,t,s} - X_{\mathcal{P}_i,s}\ell^{*}_{\mathcal{P}_i i,t,s}\big),\;\; i\in\mathcal{B}^{\mathrm{D}},\forall t,s, \tag{1k}$$

$$v^{*}_{j,t,s} = v^{*}_{i,t,s} - 2\big(R_{ij,s}p^{*}_{ij,t,s} + X_{ij,s}q^{*}_{ij,t,s}\big) + \big(R^2_{ij,s} + X^2_{ij,s}\big)\ell^{*}_{ij,t,s},\;\; ij\in\mathcal{L}^{\mathrm{D}},\forall t,s, \tag{1l}$$

$$0 \le \ell^{*}_{ij,t,s} \le \overline{L}^2_{ij,s},\;\; ij\in\mathcal{L}^{\mathrm{D}},\forall t,s, \tag{1m}$$

$$\underline{V}^2_{i,s} \le v^{*}_{i,t,s} \le \overline{V}^2_{i,s},\;\; i\in\mathcal{B}^{\mathrm{D}},\forall t,s, \tag{1n}$$

$$0 \le p^{\mathrm{FFR}}_{i,t,s} \le \overline{P}^{\mathrm{FFR}}_{i,s},\;\; i\in\mathcal{G}^{\mathrm{D}},\forall t,s, \tag{1o}$$

$$\underline{P}_{i,s} \le p_{i,t,s} + p^{\mathrm{FFR}}_{i,t,s} \le \overline{P}_{i,s},\;\; i\in\mathcal{G}^{\mathrm{D}},\forall t,s, \tag{1p}$$

$$\left\|\begin{matrix} 2p^{*}_{ij,t,s} \\ 2q^{*}_{ij,t,s} \\ \ell^{*}_{ij,t,s} - v^{*}_{i,t,s}\end{matrix}\right\|_2 \le \ell^{*}_{ij,t,s} + v^{*}_{i,t,s},\;\; ij\in\mathcal{L}^{\mathrm{D}},\forall t,s, \tag{1q}$$

The corresponding LL TN market-clearing problem is formulated as follows:

$$\min_{\Xi^{\mathrm{LL}}} \sum_{t\in\mathcal{T}}\Bigg(\sum_{i\in\mathcal{G}^{\mathrm{T}}}\big(C_{i,t}p_{i,t} + C^{\mathrm{PFR}}_{i,t}p^{\mathrm{PFR}}_{i,t}\big) - \sum_{s\in\mathcal{I}}\big(C_{0,t,s}p_{0,t,s} + C^{\mathrm{FFR}}_{0,t,s}p^{\mathrm{FFR}}_{0,t,s}\big)\Bigg) \tag{2a}$$

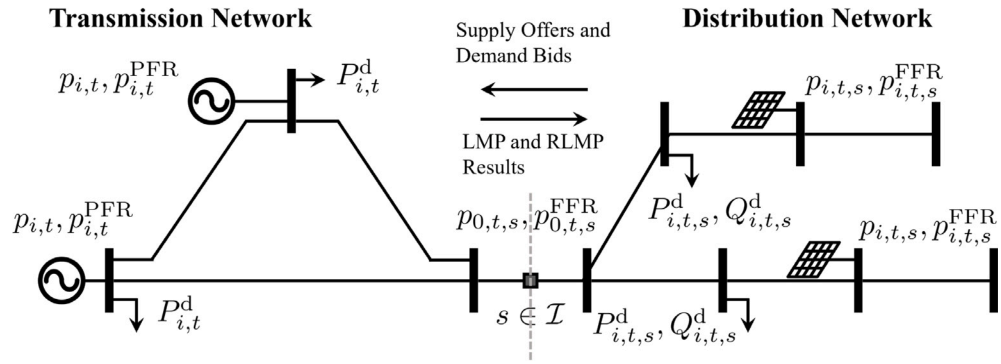

Fig. 2. Integrated structure of the transmission and distribution networks.

$$\text{s.t.} \sum_{i\in\mathcal{G}^{\mathrm{T}}} p_{i,t} - \sum_{s\in\mathcal{I}} p_{0,t,s} - \sum_{i\in\mathcal{D}^{\mathrm{T}}} P_{i,t}^{\mathrm{d}} = 0, \quad : \Upsilon_t, \ \forall t, \tag{2b}$$

$$\underline{P}_i \le p_{i,t} \le \overline{P}_i, \quad : \underline{\Phi}_{i,t}, \overline{\Phi}_{i,t}, \quad i \in \mathcal{G}^{\mathrm{T}}, \forall t, \tag{2c}$$

$$\begin{aligned} -\overline{L}_l \le & \sum_{i\in\mathcal{G}^{\mathrm{T}}} \gamma_{li} p_{i,t} - \sum_{s\in\mathcal{I}} \gamma_{ls} p_{0,t,s} \\ & - \sum_{i\in\mathcal{D}^{\mathrm{T}}} \gamma_{li} P_{i,t}^{\mathrm{d}} \le \overline{L}_l, \quad : \underline{\Psi}_{l,t}, \overline{\Psi}_{l,t}, \quad l \in \mathcal{L}^{\mathrm{T}}, \forall t, \end{aligned} \tag{2d}$$

$$0 \le p_{i,t}^{\mathrm{PFR}} \le \overline{P}_i^{\mathrm{PFR}}, \quad : \underline{\Omega}_{i,t}^*, \overline{\Omega}_{i,t}^*, \quad i \in \mathcal{G}^{\mathrm{T}}, \forall t, \tag{2e}$$

$$\underline{P}_i \le p_{i,t} + p_{i,t}^{\mathrm{PFR}} \le \overline{P}_i, \quad : \underline{\Phi}_{i,t}^*, \overline{\Phi}_{i,t}^*, \quad i \in \mathcal{G}^{\mathrm{T}}, \forall t, \tag{2f}$$

$$\begin{aligned} -\overline{L}_l \le & \sum_{i\in\mathcal{G}^{\mathrm{T}}} \gamma_{li} (p_{i,t} + p_{i,t}^{\mathrm{PFR}}) \\ & - \sum_{s\in\mathcal{I}} \gamma_{ls} (p_{0,t,s} + p_{0,t,s}^{\mathrm{FFR}}) \\ & - \sum_{i\in\mathcal{D}^{\mathrm{T}}} \gamma_{li} P_{i,t}^{\mathrm{d}} \le \overline{L}_l, \quad : \underline{\Psi}_{l,t}^*, \overline{\Psi}_{l,t}^* \quad l \in \mathcal{L}^{\mathrm{T}}, \forall t, \end{aligned} \tag{2g}$$

$$\begin{aligned} & \left\| \begin{bmatrix} \frac{1}{f_0} & \frac{-t^{\mathrm{FFR}}}{4\overline{\Delta f}} & \frac{-1}{t^{\mathrm{PFR}}} & 0 \\ 0 & \frac{-1}{\sqrt{\overline{\Delta f}}} & 0 & \frac{1}{\sqrt{\overline{\Delta f}}} \end{bmatrix} \begin{bmatrix} H_t^{\mathrm{sys}} \\ -\sum_{s\in\mathcal{I}} p_{0,t,s}^{\mathrm{FFR}} \\ \sum_{i\in\mathcal{G}^{\mathrm{T}}} p_{i,t}^{\mathrm{PFR}} \\ P_t^{\mathrm{loss}} \end{bmatrix} \right\|_2 \\ & \le \begin{bmatrix} \frac{1}{f_0} & \frac{-t^{\mathrm{FFR}}}{4\overline{\Delta f}} & \frac{1}{t^{\mathrm{PFR}}} & 0 \end{bmatrix} \begin{bmatrix} H_t^{\mathrm{sys}} \\ -\sum_{s\in\mathcal{I}} p_{0,t,s}^{\mathrm{FFR}} \\ \sum_{i\in\mathcal{G}^{\mathrm{T}}} p_{i,t}^{\mathrm{PFR}} \\ P_t^{\mathrm{loss}} \end{bmatrix}, \\ & : \Lambda_t^{\mathrm{a}}, \Lambda_t^{\mathrm{b}}, \Pi_t, \quad \forall t, \end{aligned} \tag{2h}$$

where the UL and LL decision-variable sets are $\Xi^{\mathrm{UL}} := \{p_{i,t,s}, q_{i,t,s}, v_{i,t,s}, p_{i,t,s}^{\mathrm{FFR}}, p_{ij,t,s}, q_{ij,t,s}, \ell_{ij,t,s}, v_{i,t,s}^*, p_{ij,t,s}^*, q_{ij,t,s}^*, \ell_{ij,t,s}^*\}$, $\Xi^{\mathrm{LL}} := \{p_{i,t}, p_{i,t}^{\mathrm{PFR}}, p_{0,t,s}, p_{0,t,s}^{\mathrm{FFR}}\}$. Here, $p_{0,t,s}$ and $p_{0,t,s}^{\mathrm{FFR}}$ denote the energy and reserve transactions at PCC s. They appear in the objective functions and constraints of both the TN and DN models. In the DN model, they are represented at the PCC bus indexed by $i = 0$. In each constraint, the symbols following the equations denote the associated dual variables.

The objective function (1a) of the UL model is formulated to minimize the operating cost of the DN, including energy and reserve interactions with the TN. Constraints (1b)–(1i) model the base-case DN operating point using a standard SOCP-based branch-flow AC-OPF, whereas constraints (1j)–(1q) describe the reserve-activation DN operating point using the same branch-flow model and operating limits. The starred variables represent the post-FFR feeder states. In the LL model, objective function (2a) minimizes the operating cost of the TN, reflecting energy and reserve coordination with connected DNs. Constraints (2b)–(2d) correspond to energy scheduling in the TN and follow a standard generation shift factor (GSF)-based DC-OPF formulation. Constraints (2e)–(2g) describe reserve scheduling in the TN, namely PFR capacity limits, post-reserve generator output limits, and post-activation transmission line-flow limits, respectively.

Constraint (2h) is a SOC-based frequency-security constraint that enforces the frequency-nadir requirement, following the governor-rate-constrained adequacy formulation in [36] and the closed-form frequency-security formulations in [17,18]. It uses the system inertia (H_t^{sys}), the size of the largest loss (P_t^{loss}), the maximum allowable frequency deviation ($\overline{\Delta f}$), and the committed FFR and PFR quantities and delivery times. In the present model, H_t^{sys} and P_t^{loss} are treated as predetermined hourly security inputs. For each hour, one representative largest-loss unit is selected, and the tripped unit is excluded from both the PFR procurement and the inertia contribution in (2h). Each reserve service is modeled as a linear ramp from zero to its committed quantity over its delivery time, so explicit droop coefficients are not required. Distribution-side FFR enters (2h) through the PCC-aggregated quantity $\sum_{s\in\mathcal{I}} p_{0,t,s}^{\mathrm{FFR}}$, is assumed to remain available under the generator-outage contingency, and its deliverability within each DN is enforced by constraints (1j)–(1q). Rate of change of frequency (RoCoF) is not imposed as a separate algebraic constraint in the clearing model and is instead evaluated ex post in the case studies using time-domain simulations.

The PCC LMP and RLMP are obtained from the LL dual variables as

$$\pi_{0,t,s}^{\mathrm{LMP}} = -\Upsilon_t + \sum_{l\in\mathcal{L}^{\mathrm{T}}} \gamma_{ls} (\underline{\Psi}_{l,t} - \overline{\Psi}_{l,t} + \underline{\Psi}_{l,t}^* - \overline{\Psi}_{l,t}^*) \tag{3a}$$

$$\pi_{0,t,s}^{\mathrm{RLMP}} = \sum_{l\in\mathcal{L}^{\mathrm{T}}} \gamma_{ls} (\underline{\Psi}_{l,t}^* - \overline{\Psi}_{l,t}^*) - \frac{t^{\mathrm{FFR}}}{4\overline{\Delta f}} (\Lambda_t^{\mathrm{a}} + \Pi_t) - \frac{\Lambda_t^{\mathrm{b}}}{\sqrt{\overline{\Delta f}}} \tag{3b}$$

Because H_t^{sys} is treated as an exogenous security input from an external unit-commitment schedule rather than a traded decision variable, the present lower-level clearing does not include a separate inertia product or inertia price. Unit start-up and shut-down decisions therefore affect the reserve-clearing outcomes only indirectly through the hourly values of H_t^{sys} and P_t^{loss}. The reported RLMP reflects the marginal value of deliverable frequency response at the PCC under those fixed commitment-dependent conditions.

4. Solution methods

The proposed optimal scheduling model has a hierarchical structure and exhibits non-convex characteristics. Therefore, the LL model is first reformulated using the KKT optimality conditions, converting the bi-level problem into a single-level MPEC problem. Subsequently, two linearization techniques are applied to transform the model into a MISOCP formulation, and penalty coefficients are introduced to minimize the SOC relaxation gap, resulting in the final tractable optimization model.

4.1. MPEC reformulation

The KKT optimality conditions of the LL model can be utilized to equivalently transform it into a single-level MPEC problem as follows:

$$\min_{\Xi^{\mathrm{SL}}} \quad (1a) \tag{4a}$$

$$\text{s.t.} \quad (1b) - (1q),\ (2b) - (2h), \tag{4b}$$

$$C_{i,t} + \Upsilon_t - \underline{\Phi}_{i,t} + \overline{\Phi}_{i,t} - \underline{\Phi}^*_{i,t} + \overline{\Phi}^*_{i,t} - \sum_{l\in\mathcal{L}^{\mathrm{T}}} \gamma_{li}(\underline{\Psi}_{l,t} - \overline{\Psi}_{l,t} + \underline{\Psi}^*_{l,t} - \overline{\Psi}^*_{l,t}) = 0, i \in \mathcal{G}^{\mathrm{T}}, \forall t, \tag{4c}$$

$$C^{\mathrm{PFR}}_{i,t} - \underline{\Omega}^*_{i,t} + \overline{\Omega}^*_{i,t} - \underline{\Phi}^*_{i,t} + \overline{\Phi}^*_{i,t} + \frac{\Lambda^{\mathrm{a}}_t}{t^{\mathrm{PFR}}} - \frac{\Pi_t}{t^{\mathrm{PFR}}} - \sum_{l\in\mathcal{L}^{\mathrm{T}}} \gamma_{li}(\underline{\Psi}^*_{l,t} - \overline{\Psi}^*_{l,t}) = 0, \quad i \in \mathcal{G}^{\mathrm{T}}, \forall t, \tag{4d}$$

$$\left\| \Lambda^{\mathrm{a}}_t \quad \Lambda^{\mathrm{b}}_t \right\|_2 \le \Pi_t, \quad \forall t, \tag{4e}$$

$$0 \le (p_{i,t} - \underline{P}_i) \perp \underline{\Phi}_{i,t} \ge 0, \quad i \in \mathcal{G}^{\mathrm{T}}, \forall t, \tag{4f}$$

$$0 \le (\overline{P}_i - p_{i,t}) \perp \overline{\Phi}_{i,t} \ge 0, \quad i \in \mathcal{G}^{\mathrm{T}}, \forall t, \tag{4g}$$

$$0 \le (\sum_{i\in\mathcal{G}^{\mathrm{T}}} \gamma_{li} p_{i,t} - \sum_{s\in\mathcal{I}} \gamma_{ls} p_{0,t,s} - \sum_{i\in\mathcal{D}^{\mathrm{T}}} \gamma_{li} P^{\mathrm{d}}_{i,t} + \overline{L}_l) \perp \underline{\Psi}_{l,t} \ge 0, \quad l \in \mathcal{L}^{\mathrm{T}}, \forall t, \tag{4h}$$

$$0 \le (-\sum_{i\in\mathcal{G}^{\mathrm{T}}} \gamma_{li} p_{i,t} + \sum_{s\in\mathcal{I}} \gamma_{ls} p_{0,t,s} + \sum_{i\in\mathcal{D}^{\mathrm{T}}} \gamma_{li} P^{\mathrm{d}}_{i,t} + \overline{L}_l) \perp \overline{\Psi}_{l,t} \ge 0, \quad l \in \mathcal{L}^{\mathrm{T}}, \forall t, \tag{4i}$$

$$0 \le p^{\mathrm{PFR}}_{i,t} \perp \underline{\Omega}^*_{i,t} \ge 0, \quad i \in \mathcal{G}^{\mathrm{T}}, \forall t, \tag{4j}$$

$$0 \le (\overline{P}^{\mathrm{PFR}}_i - p^{\mathrm{PFR}}_{i,t}) \perp \overline{\Omega}^*_{i,t} \ge 0, \quad i \in \mathcal{G}^{\mathrm{T}}, \forall t, \tag{4k}$$

$$0 \le (p_{i,t} + p^{\mathrm{PFR}}_{i,t} - \underline{P}_i) \perp \underline{\Phi}^*_{i,t} \ge 0, \quad i \in \mathcal{G}^{\mathrm{T}}, \forall t, \tag{4l}$$

$$0 \le (\overline{P}_i - p_{i,t} - p^{\mathrm{PFR}}_{i,t}) \perp \overline{\Phi}^*_{i,t} \ge 0, \quad i \in \mathcal{G}^{\mathrm{T}}, \forall t, \tag{4m}$$

$$0 \le \sum_{i\in\mathcal{G}^{\mathrm{T}}} \gamma_{li}(p_{i,t} + p^{\mathrm{PFR}}_{i,t}) - \sum_{s\in\mathcal{I}} \gamma_{ls}(p_{0,t,s} + p^{\mathrm{FFR}}_{0,t,s}) - \sum_{i\in\mathcal{D}^{\mathrm{T}}} \gamma_{li}(P^{\mathrm{d}}_{i,t} + \overline{L}_l) \perp \underline{\Psi}^*_{l,t} \ge 0, \quad l \in \mathcal{L}^{\mathrm{T}}, \forall t, \tag{4n}$$

$$0 \le -\sum_{i\in\mathcal{G}^{\mathrm{T}}} \gamma_{li}(p_{i,t} + p^{\mathrm{PFR}}_{i,t}) + \sum_{s\in\mathcal{I}} \gamma_{ls}(p_{0,t,s} + p^{\mathrm{FFR}}_{0,t,s}) + \sum_{i\in\mathcal{D}^{\mathrm{T}}} \gamma_{li}(P^{\mathrm{d}}_{i,t} + \overline{L}_l) \perp \overline{\Psi}^*_{l,t} \ge 0, \quad l \in \mathcal{L}^{\mathrm{T}}, \forall t, \tag{4o}$$

where the single-level model includes all decision variables from both the UL and LL models, as well as the dual variables associated with the LL model.

The complementary constraint of SOC constraint (2h) represents a significant challenge in converting the model into an MPEC. However, if the SOC relaxation gap is negligible, the complementary constraint of the SOC constraint can be considered already satisfied [37]. In this model, owing to the minimal SOC relaxation gap of (2h), the complementary constraint can be ignored, as validated in Section 5.4.2.

4.2. Transformation to MISOCP

4.2.1. Linearization of complementary constraints

The complementary constraints of the MPEC reformulation model can be relaxed using the Big-M method, as follows:

$$0 \le a \perp b \ge 0 \rightarrow a \ge 0, b \ge 0, a \le M(1-u), b \le Mu \tag{5}$$

where M is a sufficiently large value, and u is a binary variable. Through this, constraints (4f)–(4o) can be linearized.

4.2.2. Linearization of bilinear terms

The objective function of the MPEC reformulation model consists of bilinear terms $\pi^{\mathrm{LMP}}_{0,t,s} p_{0,t,s}$ and $\pi^{\mathrm{RLMP}}_{0,t,s} p^{\mathrm{FFR}}_{0,t,s}$, which are non-convex. These terms are linearized using strong duality theory [12]. As this theory ensures that the objective function values of the primal and dual problems in the LL problem are identical, the objective function of the MPEC reformulation model is transformed as follows:

$$\begin{aligned}\min_{\Xi^{\mathrm{SL}}} \sum_{t\in\mathcal{T}} \Bigg(& \sum_{i\in\mathcal{G}^{\mathrm{T}}} (C_{i,t} p_{i,t} + C^{\mathrm{PFR}}_{i,t} p^{\mathrm{PFR}}_{i,t}) \\ & + \sum_{i\in\mathcal{D}^{\mathrm{T}}} P^{\mathrm{d}}_{i,t} \Big(\Upsilon_t - \sum_{l\in\mathcal{L}^{\mathrm{T}}} \gamma_{li}(\underline{\Psi}_{l,t} - \overline{\Psi}_{l,t} + \underline{\Psi}^*_{l,t} - \overline{\Psi}^*_{l,t})\Big) \\ & + \sum_{i\in\mathcal{G}^{\mathrm{T}}} \overline{\Omega}^*_{i,t} \overline{P}^{\mathrm{PFR}}_i - \sum_{i\in\mathcal{G}^{\mathrm{T}}} \Big((\underline{\Phi}_{i,t} + \underline{\Phi}^*_{i,t}) \underline{P}_i - (\overline{\Phi}_{i,t} + \overline{\Phi}^*_{i,t}) \overline{P}_i \Big) \\ & + \sum_{l\in\mathcal{L}^{\mathrm{T}}} \Big((\underline{\Psi}_{l,t} + \overline{\Psi}_{l,t} + \underline{\Psi}^*_{l,t} + \overline{\Psi}^*_{l,t}) \overline{L}_l \Big) \\ & + \frac{H^{\mathrm{sys}}_t}{f_0} \Big(\Lambda^{\mathrm{a}}_t + \Pi_t \Big) + \frac{P^{\mathrm{loss}}_t}{\sqrt{\Delta f}} \Lambda^{\mathrm{b}}_t \\ & + \sum_{s\in\mathcal{I}} \sum_{i\in\mathcal{G}^{\mathrm{D}}} \Big(C_{i,t,s} p_{i,t,s} + C^{\mathrm{FFR}}_{i,t,s} p^{\mathrm{FFR}}_{i,t,s} \Big) \Bigg). \end{aligned} \tag{6}$$

A step-by-step derivation of Eq. (6) for the convex LL SOCP is provided in Appendix.

4.3. Final single-level model based on SOC relaxation gap recovery

The SOCP-based AC-OPF formulation is a relaxed form in which quadratic constraints are converted into SOC constraints. As a result, the feasible region of the optimization problem expands, potentially leading to an SOC relaxation gap that may reduce the accuracy of the model. Moreover, this inexactness becomes more pronounced when the optimal solution lies at the upper bounds of current or voltage variables [38,39]. Therefore, this issue must be addressed to accurately represent network constraints in the system operation model. To overcome this challenge, a penalty term is introduced [37,40], as follows:

$$\min_{\Xi^{\mathrm{SL}}} \quad (6) + \epsilon \sum_{t\in\mathcal{T}} \sum_{s\in\mathcal{I}} \sum_{ij\in\mathcal{L}^{\mathrm{D}}} (\varphi_{ij,t,s} + \varphi^*_{ij,t,s}) \tag{7a}$$

$$\text{s.t.} \quad (4b) - (4e), \tag{7b}$$

$$\text{The linear form of } (4f) - (4o), \tag{7c}$$

where $\varphi_{ij,t,s}$ and $\varphi^*_{ij,t,s}$ are respectively defined as $\ell_{ij,t,s} + \upsilon_{i,t,s}$ and $\ell^*_{ij,t,s} + \upsilon^*_{i,t,s}$. Additionally, ϵ is the penalty coefficient, which is selected by balancing the trade-off between the accuracy of the model and the minimization of system operating costs.

5. Case studies

5.1. Test data and implementation

This section considers two integrated TN–DN test systems. Case Study I uses an IEEE 14-bus TN connected to two IEEE 33-bus DNs, as shown in Fig. 3(a), to isolate the effects of FFR introduction and to examine the feasibility of coordinated TN–DN operation under network constraints. Cases 1–3 are conducted on this system. Case Study II uses an expanded IEEE 39-bus TN connected to ten IEEE 33-bus DNs, as shown in Fig. 3(b), to investigate large-scale multi-DN coordination and the scalability of the proposed formulation. Case 4 is conducted on this system. Representative generator and DER groups used in the IEEE 14-bus TN, IEEE 39-bus TN, and IEEE 33-bus DN systems are summarized in Table 2.

The hourly scaling factors in Fig. 4 are applied to load, PV generation, and the base offer prices of energy and reserve to construct

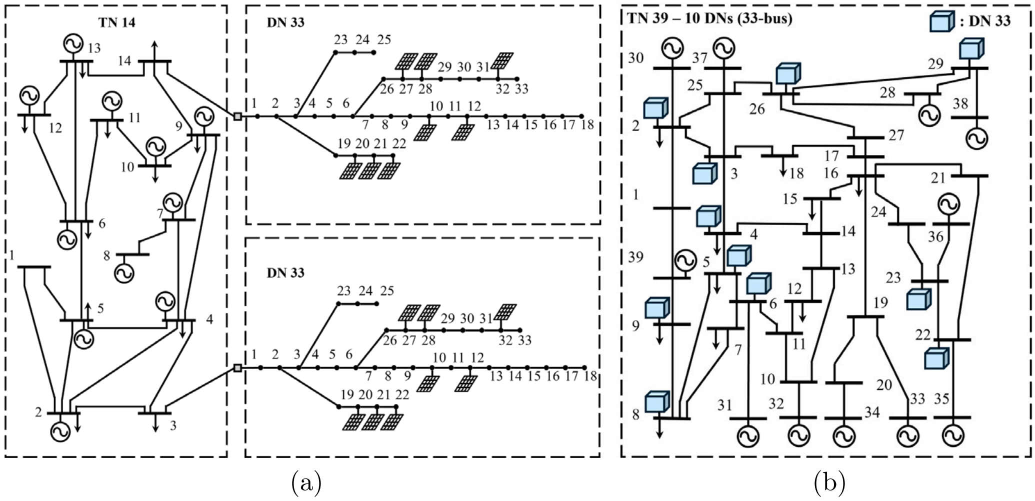

Fig. 3. Test systems for the case studies: (a) IEEE 14-bus TN with two IEEE 33-bus DNs for Cases 1–3; (b) IEEE 39-bus TN with ten IEEE 33-bus DNs for Case 4.

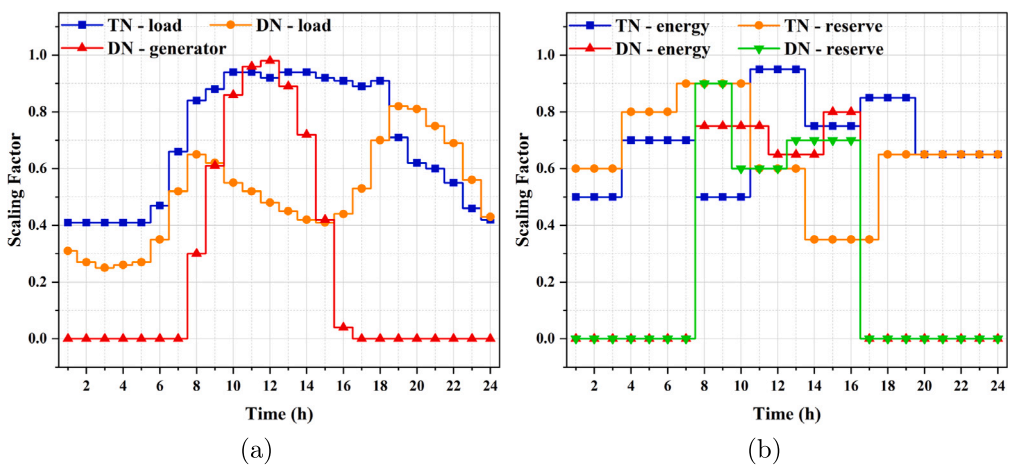

Fig. 4. Hourly scaling factors used to construct the day-ahead datasets: (a) load and PV generation, (b) energy and reserve offer prices.

Table 2
Representative generator and DER groups used in the test systems.

	Number	Min P (MW)	Max P (MW)	Base Offer Price ($/MW)		Inertia Constant (s)
				Energy	Reserve	
TN 14	4	10	100	30	15	10
	4	10	80	35	17.5	9
	3	10	50	40	20	8
TN 39	3	10	100	35	17.5	10
	5	10	80	40	20	9
	3	10	50	45	22.5	8
DN 33	2	0	1.5	15	7.5	0
	2	0	1	20	10	0
	2	0	0.5	25	12.5	0
	2	0	0.2	30	15	0

day-ahead datasets over a common 24 h horizon. Differences among the test networks are retained through their own demand levels, resource capacities, and network data. The hourly load and PV profiles in Fig. 4(a) were derived from the public datasets in [41,42]. In the case studies, PV-based DER availability follows forecasted day-ahead profiles. The cleared DN-side energy and FFR schedules should therefore be interpreted under the assumed PV availability.

The base energy and reserve offer prices in Table 2 are benchmark values used to construct the hourly offer curves in Fig. 4(b). The reserve offer prices were set relative to the corresponding energy offer prices. The inertia constants in Table 2 are representative values selected with reference to prior studies [43]. The nominal frequency is set to 60 Hz, the maximum allowable frequency deviation is set to 1.0 Hz, and the delivery times of FFR and PFR are set to 0.25 s [44,45] and 8 s, respectively.

In the case studies, system inertia was calculated as the sum of the products of inertia constant and rated capacity for the online synchronous generators except the selected largest-loss unit. Inertia contributions from DERs were not considered. The hourly largest-loss input followed the $N-1$ definition given in Section 3. If multiple

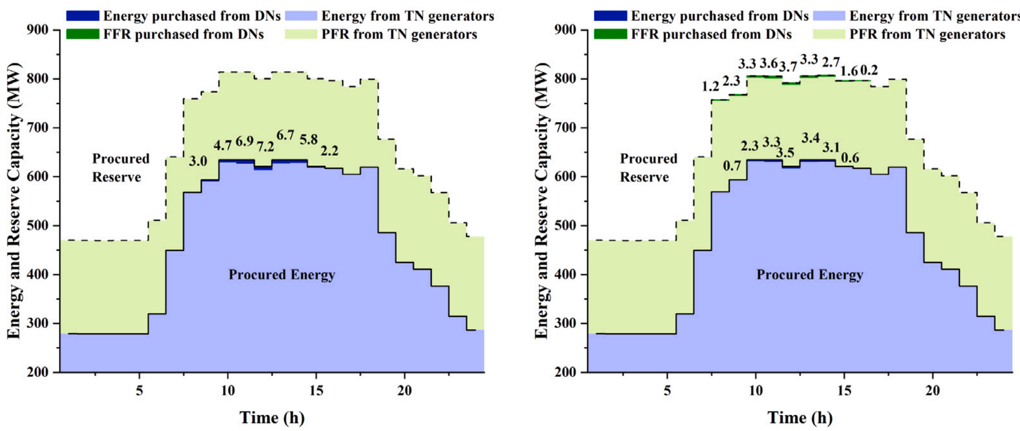

(a) (b)

Fig. 5. TN-side energy and reserve procurement schedules in case study I: (a) Case 1, (b) Case 2.

Table 3
Hourly FR requirements in case study I with and without DN-side FFR (system inertia treated as an exogenous input)

Time (h)	System Inertia (GW s)	Case 1	Case 2		Ratio of FR in Cases 1 and 2
		PFR (MW)	PFR (MW)	FFR (MW)	
7	6.28	191.08	191.08	0.00	1.00
8	6.28	191.08	186.82	1.16	0.98
9	6.68	179.64	171.55	2.34	0.97
10	6.68	179.64	168.30	3.30	0.96
11	6.68	179.64	167.31	3.59	0.95
12	6.68	179.64	167.06	3.66	0.95
13	6.68	179.64	168.19	3.33	0.95
14	6.68	179.64	170.35	2.69	0.96
15	6.68	179.64	174.11	1.60	0.98
16	6.68	179.64	179.10	0.16	1.00
17	6.68	179.64	179.64	0.00	1.00

online units had the same largest rated capacity, one representative unit was selected. The selected unit was not allowed to provide PFR and did not contribute to the system inertia calculation. The optimal operation model is formulated as a MISOCP, implemented in Python, and solved using Gurobi 12.0.1 on a workstation with an Intel i9-13900K CPU and 64 GB of RAM. To separately assess the value of FFR, the impact of network constraints, and the scalability of coordinated TN–DN scheduling, the following four cases are considered.

Case 1: Joint energy and PFR scheduling with network constraints.

Case 2: Joint energy, PFR, and FFR co-scheduling with network constraints.

Case 3: Joint energy, PFR, and FFR co-scheduling with relaxed feeder-level DN constraints.

Case 4: Joint energy, PFR, and FFR co-scheduling with network constraints on the expanded TN–multi-DN system.

All four cases are solved under the same SOC-based frequency-security formulation in (2h), while the case variations concern the availability of DN-side FFR, the treatment of DN feeder feasibility, and the system scale. Cases 1, 2, and 4 are the network-feasible cases used for the main operational comparisons, whereas Case 3 is included only as a benchmark to quantify the effect of neglecting feeder-level DN feasibility.

5.2. Case study I: Effects of FFR introduction and DN feasibility

Case Study I focuses on an integrated TN–DN system with one TN and two DNs. Case 1 serves as the network-feasible baseline with joint energy scheduling and TN-side PFR only. The comparison between Cases 1 and 2 isolates the effect of introducing DN-side FFR under the same network constraints. The comparison between Cases 2 and 3 uses a benchmark with relaxed feeder-level DN constraints to quantify the impact of neglecting DN network feasibility on scheduled DER support.

5.2.1. Changes in FR requirements with FFR introduction

Due to the differences in dynamic capabilities between traditional generators connected to the TN and inverter-based DERs connected to the DN, their effectiveness in arresting frequency deviations differs. Consequently, even under identical system operating conditions, the total FR requirement may vary. Fig. 5 shows the TN-side energy and reserve procurement schedule, and Table 3 reports the associated FR requirements in Cases 1 and 2. In Fig. 5, energy from TN generators and PFR from TN generators denote the contributions of TN resources. Energy purchased from DNs and FFR purchased from DNs denote the interface quantities procured from the DNs at the PCC. The most visible change between the two cases appears in the reserve composition rather than in the energy schedule. In Case 1, since DN-side FFR is not available, the FR requirement is covered solely by TN-side PFR across all time periods. In contrast, in Case 2, FFR is scheduled from DN resources during certain hours, leading to a reduction in the scheduled amount of PFR from TN resources.

The effect appears from 8 h to 16 h. During this interval, the scheduled FFR increases from 1.16 MW at 8 h to 3.66 MW at 12 h, while the required PFR decreases from 191.08 MW to 186.82 MW at 8 h and from 179.64 MW to 167.06 MW at 12 h. The reduction is most pronounced between 11 h and 13 h, when the ratio of total FR requirement falls to 0.95. At 16 h, the scheduled FFR decreases to 0.16 MW and the required PFR almost returns to the Case 1 level. At 17 h, no FFR is scheduled and the two cases become identical again.

The comparison between 7 h and 17 h also confirms that the scheduling results consistently reflect the exogenously specified inertia conditions. At 7 h, the system inertia is 6.28 GW s and the secured PFR is 191.08 MW, whereas at 17 h the system inertia increases to 6.68 GW s and the secured PFR decreases to 179.64 MW, even though no FFR is

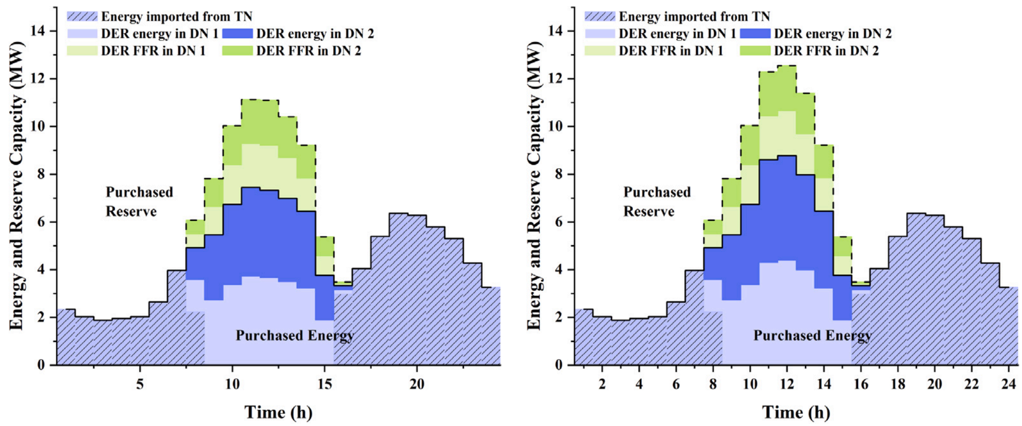

(a) (b)

Fig. 6. DN-side energy and reserve procurement schedules in case study I: (a) Case 2, (b) Case 3.

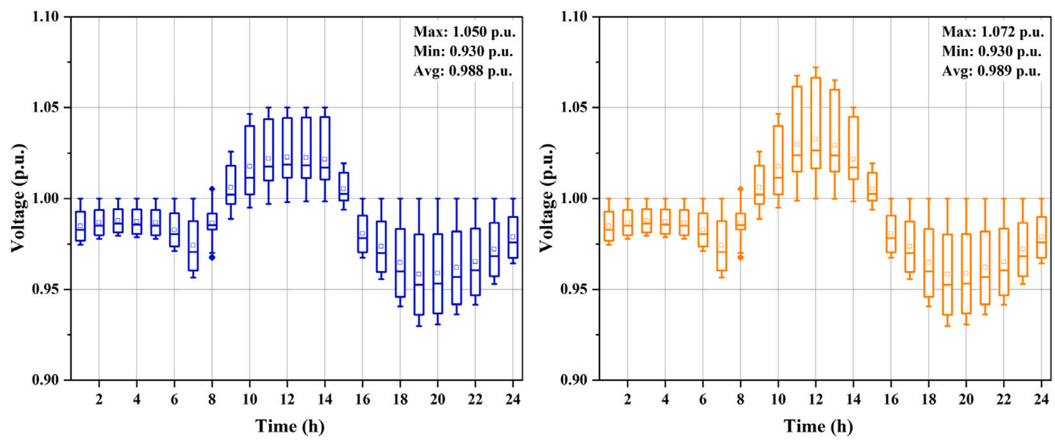

(a) (b)

Fig. 7. Hourly DN voltage profiles in case study I: (a) Case 2, (b) Case 3.

Table 4
Hourly DN-side DER energy and FFR awards in Cases 2 and 3, showing that neglecting network constraints may overestimate deliverable support.

Time (h)	Case 2		Case 3		Ratio of Energy and Reserve Cases 2 and 3
	Energy (MW)	FFR (MW)	Energy (MW)	FFR (MW)	
8	0.00	1.16	0.00	1.16	1.00
9	0.67	2.34	0.67	2.34	1.00
10	2.32	3.30	2.32	3.30	1.00
11	3.30	3.56	4.34	3.56	1.15
12	3.49	3.63	4.79	3.63	1.18
13	3.39	3.30	4.28	3.30	1.13
14	3.10	2.69	3.11	2.69	1.00
15	0.64	1.60	0.64	1.60	1.00
16	0.00	0.16	0.00	0.16	1.00

scheduled in either case. This is consistent with the intended scheduling behavior. Lower exogenous inertia leads the model to secure more PFR, while the availability of DN-side FFR allows the PFR schedule to be reduced further.

5.2.2. Impact of neglecting DN constraints on DER energy and reserve scheduling

Fig. 6 shows the DN-side energy and reserve procurement schedules in Cases 2 and 3. Table 4 summarizes the awarded DER energy and FFR. In Fig. 6, energy imported from the TN denotes the energy purchased at the PCC. The terms associated with DN 1 and DN 2 denote DER energy and DER FFR procured from DERs within each DN. When the DN is represented in aggregated form at the PCC without enforcing its internal network constraints in the scheduling process, the awarded DER support becomes larger even though the physical DN remains unchanged. The discrepancy is concentrated from 11 h to 13 h, and the ratios of Case 3 to Case 2 for the combined DN-side energy and FFR award are 1.15, 1.18, and 1.13, respectively. This should not be interpreted as additional physical DER capability. Rather, it indicates that neglecting internal DN network constraints can overestimate the deliverable support from DERs.

Table 5
Breakdown of internal costs, net PCC settlement, and operating costs for Cases 1–3 in Case Study I.

Case	TN ($)		DN ($)		Net PCC Settlement ($)	Operating cost ($)		
	PFR	Gen. Energy	FFR	DER Energy		TN	DN	Total
1	57,869	306,101	0	625	−313	363,657	938	364,595
2	56,863	306,798	97	433	11	363,672	519	364,191
3	56,862	306,675	97	470	135	363,672	432	364,104

Note: "Net PCC settlement" denotes the net transfer payment between TN and DN for energy and FFR transactions, calculated by applying the PCC LMP and RLMP to the corresponding cleared quantities and aggregating them over the study horizon. A positive value indicates a net payment from TN to DN, whereas a negative value indicates a net payment from DN to TN. Because this is an internal settlement between TN and DN, it reallocates operating cost between them but does not affect the total operating cost. The breakdown of this quantity is provided in Table 6.

Table 6
Breakdown of accumulated PCC transaction payments for Cases 1–3 in Case Study I.

Case	Energy purchased by TN from DN at PCC ($)	FFR purchased by TN from DN at PCC ($)	Energy sold by TN to DN at PCC ($)
1	1292	0	1605
2	602	1053	1644
3	731	1048	1644

Note: The "Net PCC Settlement" in Table 5 is computed as the payment for energy purchased by TN from DN at the PCC plus the payment for FFR purchased by TN from DN at the PCC, minus the payment for energy sold by TN to DN at the PCC. A positive (negative) net value indicates a payment from TN to DN (from DN to TN).

The voltage profiles in Fig. 7 explain this result. In Case 2, the maximum, minimum, and average voltages are 1.050 p.u., 0.930 p.u., and 0.988 p.u. In Case 3, these values become 1.072 p.u., 0.930 p.u., and 0.989 p.u. The relaxed case therefore produces higher midday voltages and awards that would not remain feasible under the network-feasible schedule. These results confirm that explicit DN network modeling is necessary to prevent the overestimation of DER support in coordinated TN and DN scheduling.

5.2.3. Operating cost effects of DN-side FFR introduction

Table 5 summarizes the operating cost results for Cases 1–3. The comparison between Cases 1 and 2 shows that introducing DN-side FFR lowers the total operating cost from $364,595 to $364,191 and reduces the TN internal procurement cost from $363,970 to $363,661. However, the net PCC settlement changes from −$313 to $11, which means that it changes from a net receipt from the DN to a net payment to the DN. As a result, the TN operating cost increases slightly from $363,657 to $363,672, while the DN operating cost decreases from $938 to $519.

Table 6 and Fig. 8 explain this result. The hourly PCC LMP and RLMP determine the settlement of the cleared interface energy and FFR quantities. Once DN-side FFR is introduced, part of the economic benefit appears as a change in the PCC settlement rather than as a direct reduction in the reported TN operating cost. Therefore, the slight increase in the TN operating cost should be interpreted as a PCC settlement effect, not as evidence that low-cost DN resources are ineffective. In this paper, the main contribution is not a large reduction in the TN operating cost. It is the coordinated scheduling framework that explicitly distinguishes TN-side PFR and DN-side FFR, enforces feeder-feasible delivery of DN-side FFR, and explains how the reserve mix and PCC price signals affect procurement and settlement separately.

5.3. Case study II: Expanded-system scalability and scheduling of fast and primary frequency response reserves

Case Study II considers an expanded IEEE 39-bus TN connected to ten IEEE 33-bus DNs to assess scalability and large-scale TN–DN coordination in a multi-DN setting, and to examine how hourly operating conditions are reflected in the co-optimized energy and reserve exchange schedules at the PCC and the associated PCC price signals. Time-domain validation is then performed for Case 4 to confirm that the optimized schedules satisfy the frequency-security requirements in representative hours.

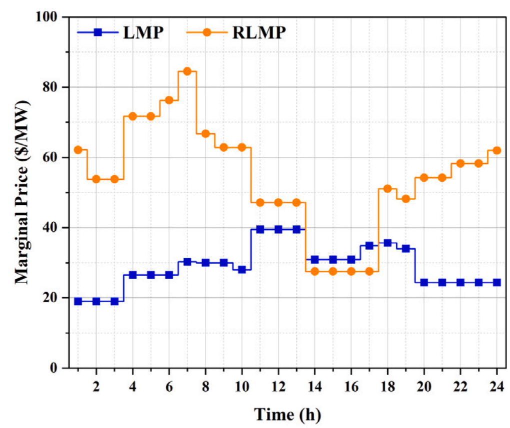

Fig. 8. PCC prices of energy and reserve in Case Study I.

5.3.1. Expanded-system scheduling results and PCC price signals

Tables 7 and 8 summarize the internal cost breakdown, the net PCC settlement, and the resulting settlement-adjusted operating costs of the expanded case. The total internal cost is $399,221, consisting of $395,567 in the TN and $3654 in the DN. On the TN side, generation energy remains the dominant internal cost component at $334,920, followed by PFR procurement at $60,647. On the DN side, the internal cost consists of $3022 for DER energy and $632 for FFR. The net PCC settlement is positive at $23,706, indicating a net payment from the TN to the DN. Therefore, the settlement-adjusted operating costs become $419,273 for the TN and −$20,052 for the DN, while the total operating cost remains unchanged at $399,221. The negative DN operating cost should be interpreted as a settlement-adjusted accounting outcome, not as a negative physical operating expense.

Table 9 reports representative scheduling results for hours 10 h to 14 h and shows how the prespecified TN operating condition is reflected in the cleared quantities and PCC prices. At 10 h, the schedule procures 124.22 MW of PFR together with 16.48 MW of DN-side FFR, with corresponding PCC LMP and RLMP of $28.00/MW and $61.78/MW, respectively. At 11 h, the prespecified TN operating condition leaves the synchronous TN units with virtually no remaining upward operating margin, so both additional energy adjustment and PFR provision become tight. Accordingly, DN-side FFR increases to 24.71 MW, while the PCC LMP and RLMP rise sharply to

Table 7
Breakdown of internal costs, net PCC settlement, and operating costs for Case 4 in Case Study II.

Case	TN ($)		DN ($)		Net PCC Settlement ($)	Operating cost ($)		
	PFR	Gen. Energy	FFR	DER Energy		TN	DN	Total
4	60,647	334,920	632	3022	23,706	419,273	−20,052	399,221

Table 8
Accumulated PCC transaction payments for Case 4 in Case Study II.

Case	Energy purchased by TN from DN at PCC ($)	FFR purchased by TN from DN at PCC ($)	Energy sold by TN to DN at PCC ($)
4	4576	29,249	10,119

Table 9
Co-optimization results for TN and DN resources and resulting PCC prices.

Time (h)	Committed Units	TN (MW)			DN (MW)		PCC ($/MW)	
		PFR	Gen. Energy	Headroom	FFR	DER Energy	LMP	RLMP
10	11	124.22	654.82	70.96	16.48	12.58	28.00	61.78
11	10	113.62	656.38	0.00	24.71	11.02	133.25	397.87
12	11	118.92	635.75	95.32	18.32	17.45	39.50	46.33
13	10	113.53	656.47	0.00	24.74	10.93	133.25	397.87
14	11	146.26	647.62	56.12	9.19	19.78	30.88	27.03

Note: A synchronous headroom of 0.00 MW at hours 11 and 13 indicates that the reserve constraints are fully binding.

Table 10
Frequency-response metrics extracted from the PSS/E validation in Case Study II.

Time (h)	System Inertia (GW s)	FFR (MW)	PFR (MW)	Nadir (Hz)	Nadir time (s)	RoCoF (0–0.5 s) (Hz/s)	RoCoF (0–1 s) (Hz/s)
10	6.80	16.48	124.22	59.003	7.725	0.201	0.064
13	6.08	24.74	113.53	59.002	7.492	0.238	0.073
17	6.80	0.00	176.47	59.008	6.117	0.227	0.078

$133.25/MW and $397.87/MW. The RLMP rises more strongly because the frequency-security reserve requirement becomes binding and the scarcity of deliverable fast reserve is reflected directly in the reserve price. A similar scarcity pattern appears at 13 h, where the RLMP again reaches $397.87/MW. By contrast, at 12 h and 14 h, more upward operating margin remains available in the synchronous TN units, as indicated by the remaining synchronous reserve capability of 95.32 MW and 56.12 MW, respectively.

Under these less tight conditions, the PCC LMP and RLMP are moderated, and the interface schedule becomes less scarcity-driven. These results show that the cleared quantities and PCC prices respond consistently to the prespecified TN operating condition. When the available upward margin in the TN becomes tight, both the PCC LMP and RLMP increase, and the RLMP responds more strongly because reserve scarcity becomes binding. When more upward margin is available, the PCC prices are moderated and larger DER energy awards become feasible.

Taken together, the cost decomposition and hourly price behavior show that the proposed coordinated TN–DN scheduling framework remains economically interpretable in the expanded multi-DN setting. When TN-side operating margins are tight, the PCC settlement becomes reserve-driven and the interface prices increase, with the reserve price responding more strongly. When the operating condition is more relaxed, the price pressure eases and larger DER energy participation becomes feasible.

5.3.2. Time-domain validation of scheduled frequency response

Fig. 9 and Table 10 present the time-domain validation results for three representative hours in Case Study II. The selected hours include two FFR-supported periods at 10 h and 13 h and one PFR-only period at 17 h. These hours were selected to highlight three distinct operating conditions. Hour 17 provides a PFR-only reference. Hour 10 allows comparison with 17 h under the same system inertia, which isolates the substitution of DN-side FFR for part of TN-side PFR. Hour 13 shows that, even under lower system inertia, scheduled FFR can replace part of slower PFR and still maintain comparable frequency security.

The dynamic simulations were carried out in PSS/E. TN generators are represented by the standard GENROU, IEEET1, TGOV1, and PSS2 A models, while converter-interfaced DERs are represented by the aggregated CBEST battery inverter model. This model is used only as a generic dynamic surrogate for converter-interfaced FFR and does not imply a battery-dominated DN resource mix. The same parameter set is retained across the tested hours to preserve comparability.

All three hours remain above 59.0 Hz at the nadir. The nadir values are 59.003 Hz at 10 h, 59.002 Hz at 13 h, and 59.008 Hz at 17 h, with corresponding nadir times of 7.725 s, 7.492 s, and 6.117 s, respectively. These results confirm that the scheduled reserves satisfy the imposed nadir requirement in all tested hours.

The activated reserve traces also illustrate the distinct dynamic roles of FFR and PFR. At 10 h and 13 h, FFR is deployed almost immediately and relieves the initial burden on PFR, whereas at 17 h the required support is supplied mainly by PFR. The comparison between 13 h and 17 h is particularly informative. Although the system inertia is lower at 13 h than at 17 h, the scheduled FFR keeps the early RoCoF close to that of 17 h. The 0–0.5 s average RoCoF is 0.238 Hz/s at 13 h and 0.227 Hz/s at 17 h, whereas the 0–1 s average RoCoF is 0.073 Hz/s at 13 h and 0.078 Hz/s at 17 h. Moreover, both hours satisfy the 59.0 Hz nadir requirement, even though the 13 h case uses a markedly different reserve mix and a lower total scheduled FR volume. The 13 h nadir is only slightly deeper, while the nadir time is delayed from 6.117 s at 17 h to 7.492 s at 13 h, indicating that fast inverter-based response can substitute for part of slower PFR and still maintain comparable frequency security. The time-domain results therefore confirm both the adequacy of the scheduled reserves and the complementary dynamic characteristics of FFR and PFR.

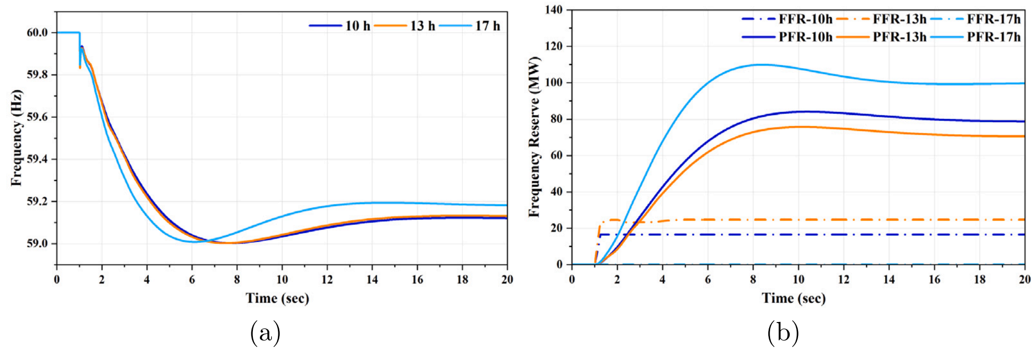

Fig. 9. PSS/E validation of scheduled frequency response in Case Study II for representative hours: (a) system frequency, (b) activated FFR and PFR at 10 h, 13 h, and 17 h.

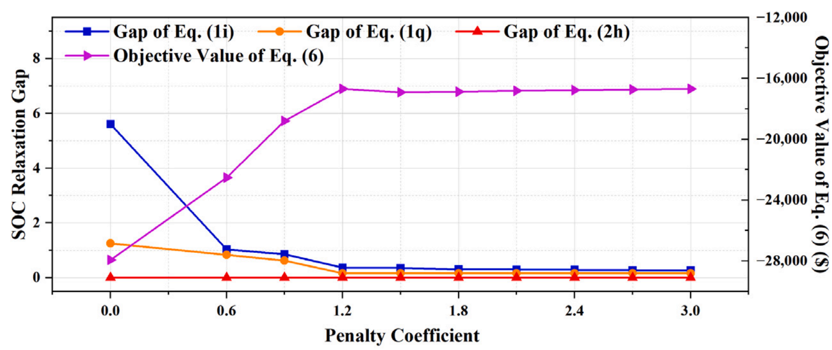

Fig. 10. Sensitivity of SOC relaxation gaps and the objective value of Eq. (6) to the penalty coefficient.

Table 11
Solver-reported computation time, model size, and final mixed-integer programming gap of the proposed MISOCP for Cases 1–4.

	Case 1	Case 2	Case 3	Case 4
Time (s)	0.85	0.93	0.93	2.02
Cont. Var.	34,376	34,376	34,376	155,936
Bin. Var.	2824	2824	2824	5284
Constraints	40,486	40,486	40,486	161,179
MIP Gap (%)	0.00	0.00	0.00	0.00

5.4. Optimality gap and SOC relaxation tightness

5.4.1. Computational performance and scalability

Table 11 reports the solver-reported computation time, model size, number of constraints, and final mixed-integer programming (MIP) gap of the proposed MISOCP for Cases 1–4. Cases 1–3, conducted on the IEEE 14-bus TN with two IEEE 33-bus DNs, are solved in 0.85–0.93 s with 34,376 continuous variables, 2824 binary variables, and 40,486 constraints. Case 4, conducted on the expanded IEEE 39-bus TN with ten IEEE 33-bus DNs, increases the model size to 155,936 continuous variables, 5284 binary variables, and 161,179 constraints, while the solver-reported computation time remains 2.02 s. The final solver-reported MIP gap is 0.00% in all cases. These results support the computational tractability of the proposed formulation for day-ahead coordinated TN–DN market clearing at the studied scale. Since the present work focuses on day-ahead scheduling rather than real-time dispatch, real-time applications and substantially larger systems would require additional acceleration strategies, which are left for future work.

5.4.2. Penalty-coefficient selection and SOC relaxation tightness

The penalty coefficient in (7a) is introduced to tighten the DN SOC relaxation. Since it is a numerical regularization parameter rather than a market parameter, it should be selected so that the relaxation gap is reduced without materially affecting the clearing solution. Fig. 10 shows the relaxation gaps of Eqs. (1i), (1q), and (2h) and the objective value of Eq. (6) for different penalty coefficients. The gap of Eq. (2h) remains zero over the tested range, while the gaps of Eqs. (1i) and (1q) decrease rapidly and become nearly unchanged at 1.2. Beyond this point, the objective value of Eq. (6) also shows no material variation. This indicates that further increasing the penalty coefficient provides no practical improvement in relaxation tightness and does not materially change the recovered objective under the tested cases. Therefore, the penalty coefficient is set to 1.2.

6. Conclusion

In the case studies, distribution-side FFR reduced the scheduled amount of transmission-side PFR, and feeder-level constraints affected the amount of distribution-side energy and reserve that could be awarded. In the reduced system, lower exogenous inertia increased the required PFR from 179.64 MW to 191.08 MW. FFR reduced total frequency-response procurement by up to 4.9%. When feeder constraints were neglected, the combined distribution-side energy and reserve award was overstated by up to 18%. In the expanded system, the largest case was solved in 2.02 s with a 0.00% optimality gap, and time-domain simulations kept the frequency nadir above 59.0 Hz in all tested hours. Overall, these results support coordinated day-ahead clearing that explicitly differentiates PFR from FFR and enforces reserve deliverability. The present study focuses on day-ahead scheduling under fixed hourly security parameters and forecasted PV availability. Future work will consider tighter coupling with commitment decisions, uncertainty-aware scheduling, broader distributed-resource portfolios, and larger-scale implementations.

CRediT authorship contribution statement

Seung-Gil Noh: Writing – original draft, Visualization, Validation, Software, Methodology, Formal analysis, Data curation, Conceptualization. **Miguel Heleno:** Writing – review & editing, Methodology, Conceptualization. **Woo Yeong Choi:** Validation, Investigation. **Yun-Su Kim:** Writing – review & editing, Methodology, Funding acquisition, Conceptualization.

Declaration of competing interest

The authors have declared no conflict of interest.

Acknowledgements

This work was supported by the Korea Institute of Energy Technology Evaluation and Planning (KETEP) and the Ministry of Trade, Industry & Energy (MOTIE) of the Republic of Korea (No. RS-2024-00394225 and No. RS-2024-00419184).

Appendix. Detailed derivation of Eq. (6) using strong duality

For notational brevity, the derivation is presented for a fixed hour t. Summing the resulting identity over all $t \in \mathcal{T}$ yields Eq. (6).

The LL problem at hour t is the following convex SOCP:

$$J_t^{\mathrm{LL}} := \min_{\Xi_t^{\mathrm{LL}}} \sum_{i\in\mathcal{G}^{\mathrm{T}}} \left(C_{i,t} p_{i,t} + C_{i,t}^{\mathrm{PFR}} p_{i,t}^{\mathrm{PFR}} \right) - \sum_{s\in\mathcal{I}} \left(C_{0,t,s} p_{0,t,s} + C_{0,t,s}^{\mathrm{FFR}} p_{0,t,s}^{\mathrm{FFR}} \right), \tag{A.1}$$

subject to (2b)–(2h). Since the objective is linear and the feasible set is described by affine constraints and one SOC constraint, the LL problem is a convex SOCP. Under Slater's condition, strong duality therefore holds.

Define

$$F_{l,t} := \sum_{i\in\mathcal{G}^{\mathrm{T}}} \gamma_{li} p_{i,t} - \sum_{s\in\mathcal{I}} \gamma_{ls} p_{0,t,s} - \sum_{i\in\mathcal{D}^{\mathrm{T}}} \gamma_{li} P_{i,t}^{\mathrm{d}}, \tag{A.2}$$

$$F_{l,t}^{*} := \sum_{i\in\mathcal{G}^{\mathrm{T}}} \gamma_{li} (p_{i,t} + p_{i,t}^{\mathrm{PFR}}) - \sum_{s\in\mathcal{I}} \gamma_{ls} (p_{0,t,s} + p_{0,t,s}^{\mathrm{FFR}}) - \sum_{i\in\mathcal{D}^{\mathrm{T}}} \gamma_{li} P_{i,t}^{\mathrm{d}}, \tag{A.3}$$

$$a_t := \frac{H_t^{\mathrm{sys}}}{f_0} + \frac{t^{\mathrm{FFR}}}{4\overline{\Delta f}} \sum_{s\in\mathcal{I}} p_{0,t,s}^{\mathrm{FFR}} - \frac{1}{t^{\mathrm{PFR}}} \sum_{i\in\mathcal{G}^{\mathrm{T}}} p_{i,t}^{\mathrm{PFR}}, \tag{A.4}$$

$$b_t := \frac{1}{\sqrt{\overline{\Delta f}}} \left(\sum_{s\in\mathcal{I}} p_{0,t,s}^{\mathrm{FFR}} + P_t^{\mathrm{loss}} \right), \tag{A.5}$$

$$c_t := \frac{H_t^{\mathrm{sys}}}{f_0} + \frac{t^{\mathrm{FFR}}}{4\overline{\Delta f}} \sum_{s\in\mathcal{I}} p_{0,t,s}^{\mathrm{FFR}} + \frac{1}{t^{\mathrm{PFR}}} \sum_{i\in\mathcal{G}^{\mathrm{T}}} p_{i,t}^{\mathrm{PFR}}, \tag{A.6}$$

so that (2h) is written compactly as

$$\left\| \begin{bmatrix} a_t \\ b_t \end{bmatrix} \right\|_2 \le c_t, \tag{A.7}$$

with the dual-cone variable $\left(\Lambda_t^{\mathrm{a}}, \Lambda_t^{\mathrm{b}}, \Pi_t\right)$ satisfying $\left\| [\Lambda_t^{\mathrm{a}} \;\; \Lambda_t^{\mathrm{b}}]^{\top} \right\|_2 \le \Pi_t$.

The LL Lagrangian is

$$\begin{aligned}
\mathcal{L}_t = J_t^{\mathrm{LL}} &+ \Upsilon_t \left(\sum_{i\in\mathcal{G}^{\mathrm{T}}} p_{i,t} - \sum_{s\in\mathcal{I}} p_{0,t,s} - \sum_{i\in\mathcal{D}^{\mathrm{T}}} P_{i,t}^{\mathrm{d}} \right) \\
&- \sum_{i\in\mathcal{G}^{\mathrm{T}}} \underline{\Phi}_{i,t} (p_{i,t} - \underline{P}_i) - \sum_{i\in\mathcal{G}^{\mathrm{T}}} \overline{\Phi}_{i,t} (\overline{P}_i - p_{i,t}) \\
&- \sum_{l\in\mathcal{L}^{\mathrm{T}}} \underline{\Psi}_{l,t} (F_{l,t} + \overline{L}_l) - \sum_{l\in\mathcal{L}^{\mathrm{T}}} \overline{\Psi}_{l,t} (-F_{l,t} + \overline{L}_l) \\
&- \sum_{i\in\mathcal{G}^{\mathrm{T}}} \underline{\Omega}_{i,t}^{*} p_{i,t}^{\mathrm{PFR}} - \sum_{i\in\mathcal{G}^{\mathrm{T}}} \overline{\Omega}_{i,t}^{*} (\overline{P}_i^{\mathrm{PFR}} - p_{i,t}^{\mathrm{PFR}}) \\
&- \sum_{i\in\mathcal{G}^{\mathrm{T}}} \underline{\Phi}_{i,t}^{*} (p_{i,t} + p_{i,t}^{\mathrm{PFR}} - \underline{P}_i) - \sum_{i\in\mathcal{G}^{\mathrm{T}}} \overline{\Phi}_{i,t}^{*} (\overline{P}_i - p_{i,t} - p_{i,t}^{\mathrm{PFR}}) \\
&- \sum_{l\in\mathcal{L}^{\mathrm{T}}} \underline{\Psi}_{l,t}^{*} (F_{l,t}^{*} + \overline{L}_l) - \sum_{l\in\mathcal{L}^{\mathrm{T}}} \overline{\Psi}_{l,t}^{*} (-F_{l,t}^{*} + \overline{L}_l) \\
&- \Lambda_t^{\mathrm{a}} a_t - \Lambda_t^{\mathrm{b}} b_t - \Pi_t c_t.
\end{aligned} \tag{A.8}$$

At the saddle point, strong duality gives $J_t^{\mathrm{LL}} = \widetilde{\mathcal{L}}_t$. Using the stationarity conditions with respect to $p_{i,t}$ and $p_{i,t}^{\mathrm{PFR}}$, i.e., (4c)–(4d), and collecting the remaining terms yields

$$\begin{aligned}
&\sum_{i\in\mathcal{G}^{\mathrm{T}}} \left(C_{i,t} p_{i,t} + C_{i,t}^{\mathrm{PFR}} p_{i,t}^{\mathrm{PFR}} \right) - \sum_{s\in\mathcal{I}} \left(C_{0,t,s} p_{0,t,s} + C_{0,t,s}^{\mathrm{FFR}} p_{0,t,s}^{\mathrm{FFR}} \right) \\
&= \sum_{s\in\mathcal{I}} p_{0,t,s} \left(-C_{0,t,s} - \Upsilon_t + \sum_{l\in\mathcal{L}^{\mathrm{T}}} \gamma_{ls} (\underline{\Psi}_{l,t} - \overline{\Psi}_{l,t} + \underline{\Psi}_{l,t}^{*} - \overline{\Psi}_{l,t}^{*}) \right) \\
&+ \sum_{s\in\mathcal{I}} p_{0,t,s}^{\mathrm{FFR}} \left(-C_{0,t,s}^{\mathrm{FFR}} + \sum_{l\in\mathcal{L}^{\mathrm{T}}} \gamma_{ls} (\underline{\Psi}_{l,t}^{*} - \overline{\Psi}_{l,t}^{*}) - \frac{t^{\mathrm{FFR}}}{4\overline{\Delta f}} \Lambda_t^{\mathrm{a}} - \frac{1}{\sqrt{\overline{\Delta f}}} \Lambda_t^{\mathrm{b}} - \frac{t^{\mathrm{FFR}}}{4\overline{\Delta f}} \Pi_t \right) \\
&+ \sum_{i\in\mathcal{D}^{\mathrm{T}}} P_{i,t}^{\mathrm{d}} \left(-\Upsilon_t + \sum_{l\in\mathcal{L}^{\mathrm{T}}} \gamma_{li} (\underline{\Psi}_{l,t} - \overline{\Psi}_{l,t} + \underline{\Psi}_{l,t}^{*} - \overline{\Psi}_{l,t}^{*}) \right) \\
&- \sum_{i\in\mathcal{G}^{\mathrm{T}}} \overline{\Omega}_{i,t}^{*} \overline{P}_i^{\mathrm{PFR}} + \sum_{i\in\mathcal{G}^{\mathrm{T}}} \left((\underline{\Phi}_{i,t} + \underline{\Phi}_{i,t}^{*}) \underline{P}_i - (\overline{\Phi}_{i,t} + \overline{\Phi}_{i,t}^{*}) \overline{P}_i \right) \\
&- \sum_{l\in\mathcal{L}^{\mathrm{T}}} \left(\underline{\Psi}_{l,t} + \overline{\Psi}_{l,t} + \underline{\Psi}_{l,t}^{*} + \overline{\Psi}_{l,t}^{*} \right) \overline{L}_l - \frac{H_t^{\mathrm{sys}}}{f_0} (\Lambda_t^{\mathrm{a}} + \Pi_t) - \frac{P_t^{\mathrm{loss}}}{\sqrt{\overline{\Delta f}}} \Lambda_t^{\mathrm{b}}.
\end{aligned} \tag{A.9}$$

Adding $\sum_{s\in\mathcal{I}} (C_{0,t,s} p_{0,t,s} + C_{0,t,s}^{\mathrm{FFR}} p_{0,t,s}^{\mathrm{FFR}})$ to both sides gives

$$\begin{aligned}
&\sum_{i\in\mathcal{G}^{\mathrm{T}}} \left(C_{i,t} p_{i,t} + C_{i,t}^{\mathrm{PFR}} p_{i,t}^{\mathrm{PFR}} \right) \\
&= \sum_{s\in\mathcal{I}} p_{0,t,s} \left(-\Upsilon_t + \sum_{l\in\mathcal{L}^{\mathrm{T}}} \gamma_{ls} (\underline{\Psi}_{l,t} - \overline{\Psi}_{l,t} + \underline{\Psi}_{l,t}^{*} - \overline{\Psi}_{l,t}^{*}) \right) \\
&+ \sum_{s\in\mathcal{I}} p_{0,t,s}^{\mathrm{FFR}} \left(\sum_{l\in\mathcal{L}^{\mathrm{T}}} \gamma_{ls} (\underline{\Psi}_{l,t}^{*} - \overline{\Psi}_{l,t}^{*}) - \frac{t^{\mathrm{FFR}}}{4\overline{\Delta f}} \Lambda_t^{\mathrm{a}} - \frac{1}{\sqrt{\overline{\Delta f}}} \Lambda_t^{\mathrm{b}} - \frac{t^{\mathrm{FFR}}}{4\overline{\Delta f}} \Pi_t \right) \\
&+ \sum_{i\in\mathcal{D}^{\mathrm{T}}} P_{i,t}^{\mathrm{d}} \left(-\Upsilon_t + \sum_{l\in\mathcal{L}^{\mathrm{T}}} \gamma_{li} (\underline{\Psi}_{l,t} - \overline{\Psi}_{l,t} + \underline{\Psi}_{l,t}^{*} - \overline{\Psi}_{l,t}^{*}) \right) \\
&- \sum_{i\in\mathcal{G}^{\mathrm{T}}} \overline{\Omega}_{i,t}^{*} \overline{P}_i^{\mathrm{PFR}} + \sum_{i\in\mathcal{G}^{\mathrm{T}}} \left((\underline{\Phi}_{i,t} + \underline{\Phi}_{i,t}^{*}) \underline{P}_i - (\overline{\Phi}_{i,t} + \overline{\Phi}_{i,t}^{*}) \overline{P}_i \right) \\
&- \sum_{l\in\mathcal{L}^{\mathrm{T}}} \left(\underline{\Psi}_{l,t} + \overline{\Psi}_{l,t} + \underline{\Psi}_{l,t}^{*} + \overline{\Psi}_{l,t}^{*} \right) \overline{L}_l - \frac{H_t^{\mathrm{sys}}}{f_0} (\Lambda_t^{\mathrm{a}} + \Pi_t) - \frac{P_t^{\mathrm{loss}}}{\sqrt{\overline{\Delta f}}} \Lambda_t^{\mathrm{b}}.
\end{aligned} \tag{A.10}$$

Using the price definitions in (3a)–(3b),

$$\pi_{0,t,s}^{\mathrm{LMP}} = -\Upsilon_t + \sum_{l\in\mathcal{L}^{\mathrm{T}}} \gamma_{ls} (\underline{\Psi}_{l,t} - \overline{\Psi}_{l,t} + \underline{\Psi}_{l,t}^{*} - \overline{\Psi}_{l,t}^{*}), \tag{A.11}$$

$$\pi_{0,t,s}^{\mathrm{RLMP}} = \sum_{l\in\mathcal{L}^{\mathrm{T}}} \gamma_{ls} (\underline{\Psi}_{l,t}^{*} - \overline{\Psi}_{l,t}^{*}) - \frac{t^{\mathrm{FFR}}}{4\overline{\Delta f}} (\Lambda_t^{\mathrm{a}} + \Pi_t) - \frac{1}{\sqrt{\overline{\Delta f}}} \Lambda_t^{\mathrm{b}}, \tag{A.12}$$

Eq. (A.10) becomes

$$\begin{aligned}
&\sum_{s\in\mathcal{I}} \left(p_{0,t,s} \pi_{0,t,s}^{\mathrm{LMP}} + p_{0,t,s}^{\mathrm{FFR}} \pi_{0,t,s}^{\mathrm{RLMP}} \right) \\
&= \sum_{i\in\mathcal{G}^{\mathrm{T}}} \left(C_{i,t} p_{i,t} + C_{i,t}^{\mathrm{PFR}} p_{i,t}^{\mathrm{PFR}} \right) - \sum_{i\in\mathcal{D}^{\mathrm{T}}} P_{i,t}^{\mathrm{d}} \left(-\Upsilon_t + \sum_{l\in\mathcal{L}^{\mathrm{T}}} \gamma_{li} (\underline{\Psi}_{l,t} - \overline{\Psi}_{l,t} + \underline{\Psi}_{l,t}^{*} - \overline{\Psi}_{l,t}^{*}) \right) \\
&+ \sum_{i\in\mathcal{G}^{\mathrm{T}}} \overline{\Omega}_{i,t}^{*} \overline{P}_i^{\mathrm{PFR}} - \sum_{i\in\mathcal{G}^{\mathrm{T}}} \left((\underline{\Phi}_{i,t} + \underline{\Phi}_{i,t}^{*}) \underline{P}_i - (\overline{\Phi}_{i,t} + \overline{\Phi}_{i,t}^{*}) \overline{P}_i \right) \\
&+ \sum_{l\in\mathcal{L}^{\mathrm{T}}} \left(\underline{\Psi}_{l,t} + \overline{\Psi}_{l,t} + \underline{\Psi}_{l,t}^{*} + \overline{\Psi}_{l,t}^{*} \right) \overline{L}_l + \frac{H_t^{\mathrm{sys}}}{f_0} (\Lambda_t^{\mathrm{a}} + \Pi_t) + \frac{P_t^{\mathrm{loss}}}{\sqrt{\overline{\Delta f}}} \Lambda_t^{\mathrm{b}}.
\end{aligned} \tag{A.13}$$

Substituting (A.13) into the UL objective (1a) and summing over $t \in \mathcal{T}$ yields Eq. (6).

Data availability

Data will be made available on request.

References

[1] Denholma P, Novacheck J, Jorgenson J, O'Connell M. Impact of Flexibility Options on Grid Economic Carrying Capacity of Solar and Wind: Three Case Studies. Golden, CO, United States: National Renewable Energy Laboratory (NREL; 2016, http://dx.doi.org/10.2172/1339345, [Online]. Available: https://www.osti.gov/biblio/1339345.

[2] Feng C, Chen Q, Wang Y, Kong P-Y, Gao H, Chen S. Provision of Contingency Frequency Services for Virtual Power Plants With Aggregated Models. IEEE Trans Smart Grid 2023;14(4):2798–811. http://dx.doi.org/10.1109/TSG.2022.3229273.

[3] Mohandes B, Moursi MSE, Hatziargyriou N, Khatib SE. A Review of Power System Flexibility With High Penetration of Renewables. IEEE Trans Power Syst 2019;34(4):3140–55. http://dx.doi.org/10.1109/TPWRS.2019.2897727.

[4] Gevorgian V, O'Neill B. Advanced grid-friendly controls demonstration project for utility-scale pv power plants. Golden, CO, United States: National Renewable Energy Lab. (NREL; 2016, http://dx.doi.org/10.2172/1236761, [Online]. Available: https://www.osti.gov/biblio/1236761.

[5] Saiz-Marin E, Garcia-Gonzalez J, Barquin J, Lobato E. Economic Assessment of the Participation of Wind Generation in the Secondary Regulation Market. IEEE Trans Power Syst 2012;27(2):866–74. http://dx.doi.org/10.1109/TPWRS.2011.2178618.

[6] Margaris ID, Papathanassiou SA, Hatziargyriou ND, Hansen AD, Sorensen P. Frequency Control in Autonomous Power Systems With High Wind Power Penetration. IEEE Trans Sustain Energy 2012;3(2):189–99. http://dx.doi.org/10.1109/TSTE.2011.2174660.

[7] Hedayati-Mehdiabadi M, Hedman KW, Zhang J. Reserve Policy Optimization for Scheduling Wind Energy and Reserve. IEEE Trans Power Syst 2018;33(1):19–31. http://dx.doi.org/10.1109/TPWRS.2017.2707568.

[8] Li H, Qiao Y, Lu Z, Zhang B, Teng F. Frequency-Constrained Stochastic Planning Towards a High Renewable Target Considering Frequency Response Support From Wind Power. IEEE Trans Power Syst 2021;36(5):4632–44. http://dx.doi.org/10.1109/TPWRS.2021.3066991.

[9] Navesi RB, Naghibi AF, Zafarani H, Tahami H, Pirouzi S. Reliable operation of reconfigurable smart distribution network with real-time pricing-based demand response. 241, 2025, 111341, [Online]. Available http://dx.doi.org/10.1016/j.epsr.2024.111341,

[10] Emdadi K, Pirouzi S. Benders decomposition-based power network expansion planning according to eco-sizing of high-voltage direct-current system, power transmission cables and renewable/non-renewable generation units. IET Renew Power Gener 2025;19(1):e70025, [Online]. Available: http://dx.doi.org/10.1049/rpg2.70025.

[11] Chen H, Fu L, Bai L, Jiang T, Xue Y, Zhang R, et al. Distribution Market-Clearing and Pricing Considering Coordination of DSOs and ISO: An EPEC Approach. IEEE Trans Smart Grid 2021;12(4):3150–62. http://dx.doi.org/10.1109/TSG.2021.3061282.

[12] Jiang T, Wu C, Zhang R, Li X, Chen H, Li G. Flexibility Clearing in Joint Energy and Flexibility Markets Considering TSO-DSO Coordination. IEEE Trans Smart Grid 2023;14(2):1376–87. http://dx.doi.org/10.1109/TSG.2022.3153634.

[13] Chen H, Wang D, Zhang R, Jiang T, Li X. Optimal participation of ADN in energy and reserve markets considering TSO-DSO interface and DERs uncertainties. Appl Energy 2022;308:118319. http://dx.doi.org/10.1016/j.apenergy.2021.118319.

[14] Arpanahi MK, Golshan MEH, Moghaddam MP. Non-cooperative Operation of Transmission and Distribution Systems. IEEE Trans Ind Inform 2022;18(1):153–62. http://dx.doi.org/10.1109/TII.2020.3041921.

[15] Badesa L, Teng F, Strbac G. Optimal Portfolio of Distinct Frequency Response Services in Low-Inertia Systems. IEEE Trans Power Syst 2020;35(6):4459–69. http://dx.doi.org/10.1109/TPWRS.2020.2997194.

[16] Badesa L, Teng F, Strbac G. Pricing inertia and Frequency Response with diverse dynamics in a Mixed-Integer Second-Order Cone Programming formulation. Appl Energy 2020;260:114334. http://dx.doi.org/10.1016/j.apenergy.2019.114334.

[17] Badesa L, Matamala C, Zhou Y, Strbac G. Assigning Shadow Prices to Synthetic Inertia and Frequency Response Reserves From Renewable Energy Sources. IEEE Trans Sustain Energy 2023;14(1):12–26. http://dx.doi.org/10.1109/TSTE.2022.3198324.

[18] Qiu D, Baig AM, Wang Y, Wang L, Jiang C, Strbac G. Market design for ancillary service provisions of inertia and frequency response via virtual power plants: A non-convex bi-level optimisation approach. Appl Energy 2024;361:122929. http://dx.doi.org/10.1016/j.apenergy.2024.122929.

[19] Zhang R, Chen Y, Yan K, Li Z, Jiang T, Li G, et al. Incorporating Frequency Security Constraints in Two-Stage Robust Unit Commitment of Integrated Transmission and Distribution System. IEEE Trans Sustain Energy 2026;17(1):70–86. http://dx.doi.org/10.1109/TSTE.2025.3593302.

[20] Jiang T, Shen Z, Jin X, Zhang R, Parisio A, Li X, et al. Solution to Coordination of Transmission and Distribution for Renewable Energy Integration into Power Grids: An Integrated Flexibility Market. CSEE J Power Energy Syst 2023;9(2):444–58. http://dx.doi.org/10.17775/CSEEJPES.2021.06390.

[21] Iria J, Scott P, Attarha A, Gordon D, Franklin E. MV-LV network-secure bidding optimisation of an aggregator of prosumers in real-time energy and reserve markets. Energy 2022;242:122962. http://dx.doi.org/10.1016/j.energy.2021.122962.

[22] Niea X, Mansouri SA, Jordehi A Rezaee, Tostado-Véliz M. A two-stage optimal mechanism for managing energy and ancillary services markets in renewable-based transmission and distribution networks by participating electric vehicle and demand response aggregators. Int J Electr Power Energy Syst 2024;158:109917, [Online]. Available:http://dx.doi.org/10.1016/j.ijepes.2024.109917.

[23] Linda L, Cossent R, Frías P. TSO-DSO interface flow pricing: a bilevel study on efficiency and cost allocation. Int J Electr Power Energy Syst 2024;161:110155, [Online]. Available: http://dx.doi.org/10.1016/j.ijepes.2024.110155.

[24] Jiang T, Wu C, Huang T, Zhang R, Li X. Optimal market participation of VPPs in TSO-DSO coordinated energy and flexibility markets. Appl Energy 2024;360:122730, [Online]. Available:http://dx.doi.org/10.1016/j.apenergy.2024.122730.

[25] Cai Q, Xu Y, Yi Z, Tu Z. TSO-DSO coordination in the joint balancing and flexibility markets considering classification and participation of VPPs. Energy 2025;335:138075, [Online]. Available:http://dx.doi.org/10.1016/j.energy.2025.138075.

[26] Hajati M, Sheikh-El-Eslami MK, Delkhosh H. Market-based bidirectional reserve and flexibility exchange in a DSO-TSO coordinated framework utilizing capability evaluation. Int J Electr Power Energy Syst 2025;172:111267, [Online]. Available: http://dx.doi.org/10.1016/j.ijepes.2025.111267.

[27] Capitanescu F. TSO–DSO interaction: Active distribution network power chart for TSO ancillary services provision. Electr Power Syst Res 2018;163(part A):226–30, [Online]. Available: http://dx.doi.org/10.1016/j.epsr.2018.06.009.

[28] Bragin MA, Dvorkin Y. TSO-DSO Operational Planning Coordination Through ℓ_1-Proximal Surrogate Lagrangian Relaxation. IEEE Trans Power Syst 2022;37(2):1274–85, [Online]. Available:http://dx.doi.org/10.1109/TPWRS.2021.3101220.

[29] Ferrandon-Cervantes CJ, Kazemtabrizi B, Troffaes MCM. Inclusion of frequency stability constraints in unit commitment using separable programming. Electr Power Syst Res 2022;203:107669, [Online]. Available:http://dx.doi.org/10.1016/j.epsr.2021.107669.

[30] Kim J, Shim JW, Shin H. A unified framework for co-optimization of PFR and FFR reserves using linearized tri-criteria frequency constraints. Int J Electr Power Energy Syst 2025;173:111392, [Online]. Available:http://dx.doi.org/10.1016/j.ijepes.2025.111392.

[31] Meng L, Zafar J, Khadem SK, Collinson A, Murchie KC, Coffele F, et al. Fast Frequency Response From Energy Storage Systems—A Review of Grid Standards, Projects and Technical Issues. IEEE Trans Smart Grid 2020;11(2):1566–81. http://dx.doi.org/10.1109/TSG.2019.2940173.

[32] Park J-S, Kim J-H, Noh S-G, Cho W-Y, Kim H-K, Kim BH, et al. Distribution System Operator (DSO) Functions in South Korea—Part I: Development, journal=Pr Obs Futur Work, international transactions on electrical energy systems. 2024;2024:1–19. http://dx.doi.org/10.1155/2024/3353622, 3353622.

[33] Lee B-H, Ahn H-H. Electricity industry restructuring revisited: the case of Korea. Energy Policy 2006;34(9):1115–26. http://dx.doi.org/10.1016/j.enpol.2004.10.002.

[34] Rita R, Marques V, Barbara D, Chaves I, Macedo P, Moutinho V, et al. Crossing non-parametric and parametric techniques for measuring the efficiency: Evidence from 65 European electricity Distribution System Operators. Energy 2023;283:128511. http://dx.doi.org/10.1016/j.energy.2023.128511.

[35] Talaeizadeh V, Shayanfar H, Aghaei J. Prioritization of transmission and distribution system operator collaboration for improved flexibility provision in energy markets. Int J Electr Power Energy Syst 2023;154:109386. http://dx.doi.org/10.1016/j.ijepes.2023.109386.

[36] H. Chávez R Baldick, Sharma S. Governor Rate-Constrained OPF for Primary Frequency Control Adequacy. IEEE Trans Power Syst 2014;29(3):1473–80. http://dx.doi.org/10.1109/TPWRS.2014.2298838.

[37] Jiang T, Yuan C, Bai L, Chowdhury B, Zhang R, Li X. Bi-Level Strategic Bidding Model of Gas-fired Units in Interdependent Electricity and Natural Gas Markets. IEEE Trans Sustain Energy 2022;13(1):328–40. http://dx.doi.org/10.1109/TSTE.2021.3110864.

[38] Jha RR, Dubey A. Exact Distribution Optimal Power Flow (D-OPF) Model using Convex Iteration Technique. In: Proc. IEEE power & energy society general meeting. PESGM, 2019, p. 1–5. http://dx.doi.org/10.1109/PESGM40551.2019.8974080.

[39] Jha RR, Inaolaji A, Biswas BD, Suresh A, Dubey A, Paudyal S, et al. Distribution Grid Optimal Power Flow (D-OPF): Modeling, Analysis, and Benchmarking. IEEE Trans Power Syst 2023;38(4):3654–68. http://dx.doi.org/10.1109/TPWRS.2022.3204227.

[40] Yang K, Wang G, Luo Z-Q. Efficient Convex Relaxation Methods for Robust Target Localization by a Sensor Network Using Time Differences of Arrivals. IEEE Trans Signal Process 2009;57(7):2775–84. http://dx.doi.org/10.1109/TSP.2009.2016891.

[41] Angizeh F, Ghofrani A, Jafari MA. Dataset on hourly load profiles for a set of 24 facilities from industrial commercial, and residential end-use sectors. Mendeley Data 2020. [Online]. Available:http://dx.doi.org/10.17632/rfnp2d3kjp.1.

[42] Koivisto MJ, Leon JP Murcia. Solar PV generation time series (PECD 2021 update). Technical University of Denmark; 2022, Dataset, [Online]. Available:http://dx.doi.org/10.11583/DTU.19727239.v1.

[43] Dimoulias SC, Kontis EO, Papagiannis GK. Inertia Estimation of Synchronous Devices: Review of Available Techniques and Comparative Assessment of Conventional Measurement-Based Approaches. Energies 2022;15(20):7767. http://dx.doi.org/10.3390/en15207767.

[44] Garcia M, Baldick R. Requirements for Interdependent Reserve Types Providing Primary Frequency Control. IEEE Trans Power Syst 2022;37(1):51–64, [Online]. Available:http://dx.doi.org/10.1109/TPWRS.2021.3094214.

[45] Brogan PV, Alikhanzadeh AH, Best RJ, Morrow DJ, Kubik ML. Fast Frequency Response Requirements for Replacement of Observed Generator Response During Under-Frequency Transients. In: Proc. CIGRE international symposium. Dublin, Ireland; 2017, p. 1–6, [Online]. Available: https://pure.qub.ac.uk/files/278944720/Fast_Frequency_Response_Requirements_for_Replacement_of_Observed_Generator_Response_During_Under_Frequency_Transients.pdf.